

1 **Interpretable Machine Learning Quantifies Composition and Size**
2 **Influences on Aerosol Spectral Absorption**

3

4 **Wenfang Wang¹, Pengfei Tian^{1,2*}, Shuhua Zeng¹, Yifei Zhang¹, Zeren Yu¹, Chen**
5 **Cui¹, Yunfei Wu³, Min Chen^{1*}, Lei Zhang^{1,2}**

6 ¹ Key Laboratory for Semi-Arid Climate Change of the Ministry of Education, College
7 of Atmospheric Sciences, Lanzhou University, Lanzhou 730000, China.

8 ² Collaborative Innovation Center for Western Ecological Safety, Lanzhou University,
9 Lanzhou 730000, China.

10 ³ State Key Laboratory of Atmospheric Environment and Extreme Meteorology,
11 Institute of Atmospheric Physics, Chinese Academy of Sciences, Beijing 100029,
12 China.

13 Corresponding author: P. Tian (tianpf@lzu.edu.cn) and M. Chen (chenmin@lzu.edu.cn)

14

15 **Abstract**

16 The spectral dependence of aerosol absorption, characterized by the absorption
17 Ångström exponent (AAE), strongly influences radiative effects, yet the relative
18 importance of controlling factors remains poorly quantified. We integrate multisource
19 observations with an interpretable machine-learning framework (Shapley Additive
20 Explanations, SHAP) to disentangle the roles of chemical composition and particle size
21 in predicting AAE and to evaluate radiative impacts. Field observation in Beijing reveal
22 that near-surface AAE is predominantly influenced by higher fine mineral dust and
23 water-soluble inorganic ions fractions. Multi-year columnar data identify dust loading
24 as the dominant predictor, followed by carbonaceous aerosols. The fine-mode radius
25 accounts for 29% of size parameters cumulative importance and ranks closely with
26 black carbon. SHAP diagnostics highlight that columnar AAE contributes to radiative
27 forcing at the top of the atmosphere (TOA) comparably to single scattering albedo
28 (SSA), while its impact is clearly weaker at the bottom of the atmosphere and in the
29 atmosphere. These findings help clarify AAE determinants and reduce uncertainties in
30 aerosol radiative effect assessments.

31

32 **1 Introduction**

33 Light-absorbing aerosols (LAAs), primarily black carbon (BC), brown carbon
34 (BrC), and mineral dust, significantly influence regional and global climate by
35 absorbing solar radiation (Bahadur et al., 2012; Cappa et al., 2016; Kok et al., 2017;
36 Nishant et al., 2019). For instance, BC contributed a net positive effective radiative
37 forcing of $0.11 \text{ W}\cdot\text{m}^{-2}$ during 1750–2019, with a wide uncertainty range from -0.20 to
38 $+0.42 \text{ W}\cdot\text{m}^{-2}$ (Intergovernmental Panel on Climate Change (Ipcc), 2023), reflecting
39 limited observational constraints on aerosol optical/microphysical properties and their
40 inaccurate representation in models (Gliß et al., 2021; Lee et al., 2016). A practical
41 diagnostic for the spectral shape of absorption is the Absorption Ångström Exponent
42 (AAE) (Ångström, 1929; Lewis et al., 2008). For pure BC, AAE is theoretically close
43 to 1.0, but observations show a range of 0.6–1.6 (Kirchstetter et al., 2004; Lack and
44 Cappa, 2010; Gyawali et al., 2012; Chakrabarty et al., 2013; Wang et al., 2021). BrC
45 and mineral dust exhibit relatively stronger absorption in the ultraviolet and visible
46 spectral wavelengths, typically yielding AAE values greater than 2.0 (Russell et al.,
47 2010; Park et al., 2018; Zhang et al., 2020; Cuesta-Mosquera et al., 2024). For example,
48 BrC AAE is frequently reported to be ~ 2 – 6 depending on source and aging, whereas
49 dust AAE is typically ~ 2 – 4 owing to shortwave absorption by iron oxides (Bergstrom
50 et al., 2007). Because AAE encodes source and process information that governs
51 aerosol absorption from ultraviolet to the near-infrared wavelength range, tighter

52 constraints on AAE can help reduce uncertainties in aerosol radiative effects (Cazorla
53 et al., 2013; Lack and Langridge, 2013; Sand et al., 2021).

54 AAE has been characterized using multiple observational approaches, including
55 in situ multi-wavelength absorption measurements and surface-based remote sensing
56 retrievals (Li et al., 2022). In situ observations provide high-precision, process-
57 resolving constraints on aerosol absorption spectra near the surface and therefore serve
58 as an important benchmark for evaluating remote sensing products and model
59 simulations (Gliß et al., 2021). In contrast, surface-based remote sensing can retrieve
60 aerosol properties integrated over the entire atmospheric column, such as Aerosol
61 Robotic Network (AERONET), enabling a broader view of aerosol spectral absorption
62 and its radiative properties (Dubovik and King, 2000). Combining in situ and column
63 retrievals is particularly valuable because they constrain complementary aspects of
64 aerosol spectral absorption. In situ measurements are sensitive to near-surface processes
65 (emissions, hygroscopic growth and aging) but have limited spatial and vertical
66 representativeness, whereas AERONET provides column-averaged constraints that are
67 directly connected to radiative impacts but can be influenced by vertical layering and
68 retrieval assumptions (Li et al., 2022). Therefore, integrating near-surface with
69 columnar AAE enables us to provide improved observational guidance for models, and
70 better constrain column characteristics relevant to radiative forcing.

71 Both near-surface and columnar AAE vary with particle size distribution, chemical
72 composition, and mixing state (Russell et al., 2010; Scarnato et al., 2013; Li et al., 2016;

73 Schuster et al., 2016a; Sotiropoulou et al., 2025). For instance, near-surface BC AAE
74 may decrease as BC cores grow or as aggregates become more compact during aging
75 processes (Liu et al., 2018). Recent numerical simulation further indicates that
76 secondary organic coatings can increase near-surface AAE, with sensitivity to coating
77 thickness (Zhang et al., 2025). In contrast, photochemical bleaching lowers BrC
78 ultraviolet absorption and near-surface AAE (Wang et al., 2019). Russell et al., (2010)
79 showed that columnar AAE values are strongly correlated with aerosol composition or
80 type. Heterogeneous aging of long-range-transported dust may enhance absorption,
81 also affecting columnar AAE (Tian et al., 2018). The magnitudes and signs of these
82 effects depend on location, season, and processing history, complicating both
83 measurements and modeling and propagating to radiative forcing uncertainty (Sand et
84 al., 2021; Li et al., 2022; Ponczek et al., 2022).

85 Studying the impact of individual factors on AAE is relatively straightforward.
86 Previous studies have already examined the effects of particle size, chemical
87 composition, and mixing state on AAE in isolation (Wu et al., 2015; Schuster et al.,
88 2016b; Li et al., 2024). However, quantitatively attributing the relative contributions of
89 particle size and chemical composition to AAE remains a challenging task due to
90 nonlinearity and collinearity among predictors. For example, observations show that
91 composition appears dominant when the shape of size distribution is quasi-stationary
92 (Utry et al., 2014), whereas Mie-theory studies highlight the role of the imaginary
93 refractive index of organics over size in explaining absorption changes (Yang et al.,

94 2025). Although these studies effectively highlight the roles of particle size and
95 chemical composition, they lack quantitative assessments of their relative importance.

96 The Shapley Additive exPlanations (SHAP) method offers a principled framework
97 for feature attribution in machine learning predictions and has been widely adopted in
98 atmospheric sciences, such as boundary-layer height inversion, ozone formation and
99 cloud-condensation-nuclei studies (Peng et al., 2023; Tao et al., 2024; Wang et al.,
100 2025a). SHAP analysis has also been applied to aerosol absorption studies to precisely
101 quantify the relative contribution of various chromophores to BrC absorption,
102 providing a mechanistic understanding of its key drivers (Wang et al., 2024). Its
103 potential to predict AAE and quantify the relative contributions of individual factors
104 remains unexplored. Addressing this gap would offer an interpretable, data-driven
105 perspective on aerosol spectral absorption.

106 This study aims to quantify the relative importance of chemical composition and
107 particle size influencing AAE using surface observations together with long-term
108 AERONET column retrievals over Beijing. We apply multiple linear regression to
109 identify their influence on near-surface AAE. Subsequently, we train an ensemble of
110 machine-learning models to predict columnar AAE. The best-performing model
111 (CatBoost) is selected for the final prediction, as described later in Section 2.4. Then
112 SHAP is used for interpretative analysis to quantify the contributions of different
113 columnar aerosol physical and chemical parameters. Finally, we also evaluate the
114 diagnostic power of columnar AAE for radiative effects, including aerosol direct

115 radiative forcing (ADRF) and radiative forcing efficiency (ARFE) using interpretable
116 machine-learning framework.

117 **2 Methods**

118 **2.1 Field Campaign and Data Processing**

119 An intensive observation campaign focusing on aerosol properties was conducted
120 in urban Beijing, China, from 16 December 2023 to 15 January 2024. Online and offline
121 instruments were deployed on the rooftop of the Institute of Atmospheric Physics,
122 Chinese Academy of Sciences (Building #3; 39.98°N, 116.39°E), approximately 45 m
123 above ground level. All online instruments were housed in a temperature-controlled
124 room maintained at ~20 °C to ensure measurement stability, and sampling lines were
125 equipped with Nafion dryers to minimize the influence of ambient humidity.

126 **2.1.1 In Situ Online Aerosol Observations**

127 Aerosol absorption coefficients ($b_{abs,\lambda}$) at 375, 532, and 870 nm were measured
128 using photoacoustic extincimeters (PAX, DMT Inc., USA). The PAX measures
129 aerosol light absorption using the photoacoustic technique, in which absorbed laser
130 energy is converted into periodic heating of the surrounding gas, generating an acoustic
131 pressure wave in an acoustic resonator that is detected by a sensitive microphone (Truex
132 and Anderson, 1979). The light absorption ($b_{abs,pax}$) can be calculated as:

$$133 \quad b_{abs,pax} = \frac{P_{mic} \times A_{res} \times \pi^2 \times f_{res}}{P_L \times (\gamma - 1) \times Q} \quad (1)$$

134 where P_{mic} and P_L are the pressure of the microphone and the laser power,
135 respectively; A_{res} , f_{res} and Q indicate the cross-sectional area, resonance frequency,
136 and quality factor of the resonator; γ is the isobaric and isosteric specific heat ratio.
137 Then the $b_{abs,\lambda}$ is obtained by subtracting the background absorption measured with
138 particle-free air from $b_{abs,pax}$. In addition, the PAX measures aerosol scattering with
139 an integrated wide-angle reciprocal nephelometer.

140 Prior to deployment, each PAX was calibrated following the procedure described
141 in Wu et al., 2015: (i) the scattering channel was calibrated using high-concentration
142 ammonium sulfate aerosol by regressing the extinction coefficient (b_{ext}) derived from
143 laser power attenuation against the instrument-recorded scattering coefficient (b_{sca}).
144 The scattering calibration factor was then adjusted by applying the regression slope as
145 a multiplicative correction; (ii) the absorption channel was calibrated using high-
146 concentration Aquadag aerosol by regressing ($b_{ext} - b_{sca}$) against the instrument-
147 recorded photoacoustic absorption. The absorption calibration factor was then updated
148 by dividing it by the regression slope.

149 The near-surface aerosol absorption Ångström exponent (AAE_{sfc}) was calculated
150 as:

$$151 \quad AAE_{sfc} = -\frac{\log(b_{abs,\lambda_1}) - \log(b_{abs,\lambda_2})}{\log(\lambda_1) - \log(\lambda_2)} \quad (2)$$

152 where $\lambda_1 = 375$ nm, $\lambda_2 = 870$ nm. Hourly $PM_{2.5}$ (particle matters with an aerodynamic
153 diameter ≤ 2.5 μ m) mass concentrations were obtained from the China National
154 Environmental Monitoring Network for the Beijing urban site. These datasets were

155 used to calculate mass absorption efficiency (MAE) of PM_{2.5}:

$$156 \quad MAE_{\lambda} = \frac{b_{abs,\lambda}}{PM_{2.5}} \quad (3)$$

157 Size distributions were measured with a scanning mobility particle sizer (SMPS,
158 Model 3082, TSI Inc., 8.8–310.6 nm, Stokes diameter) and an aerodynamic particle
159 sizer (APS, Model 3321, TSI Inc., 0.54–19.8 μm, aerodynamic diameter), with SMPS
160 data converted to aerodynamic diameter (Text S1) (Shang et al., 2018). To ensure
161 measurement accuracy, the flow systems of the SMPS and APS were periodically
162 checked and calibrated by the manufacturer (TSI Inc.) through regular return-service
163 calibration. In addition, hourly meteorological parameters (wind speed and direction,
164 temperature, and relative humidity) were obtained from the 47 m meteorological tower
165 at the Institute of Atmospheric Physics.

166 **2.1.2 Offline Aerosol Sampling**

167 Offline PM_{2.5} samples were collected on quartz-fiber filters (90 mm diameter;
168 Whatman 1855-090). Prior to sampling, quartz-fiber filters were pre-cleaned to
169 minimize filter background. Briefly, filter cassettes were rinsed with absolute ethanol
170 and air-dried, and aluminum-foil liners cut to the filter size were pre-baked at 550 °C
171 for 3 h to remove residual carbon. The quartz filters were sequentially soaked in
172 ultrapure water (5 min × 3 cycles, followed by 2 h × 2 cycles), oven-dried at 150 °C for
173 1 h, and then prebaked at 550 °C for 5 h to reduce the influence of adsorbed organic
174 and inorganic materials. After cooling, the filters were wrapped in prebaked aluminum
175 foil and conditioned for 48 h in a constant temperature and humidity environment prior

176 to gravimetric determination. Then the pre-sampling filter mass was measured using an
177 electronic microbalance (BSA124S-CW, Sartorius; readability ± 0.1 mg). Sampling was
178 conducted using a medium-volume air sampler (Model 2030, Laoshan Electronic
179 Instrument Co., Ltd.) operated at $100 \text{ L} \cdot \text{min}^{-1}$ and equipped with a $\text{PM}_{2.5}$ inlet. The inlet
180 was installed at approximately 2 m above ground level. Daytime samples were collected
181 from 09:00 to 20:30, and nighttime samples from 21:00 to 08:30 the following day.

182 After sampling, all filters were analyzed for major chemical compositions,
183 including water-soluble inorganic ions (Na^+ , K^+ , NH_4^+ , Ca^{2+} , Mg^{2+} , Cl^- , NO_3^- , and SO_4^{2-})
184 measured by ion chromatography (881 Compact IC Pro, Metrohm; and ICS-1500,
185 Dionex Inc.), metallic elements (Al, Ca, Mg, Fe, and Ti) determined by inductively
186 coupled plasma–atomic emission spectrometry (ICP-AES; iCAP 7400, Thermo), and
187 organic carbon (OC), and elemental carbon (EC) quantified using the thermal/optical
188 carbon analyzer (DRI Model 2015, USA) based on the thermal/optical reflectance
189 (TOR) method (Chow et al., 2007). The chemical analysis process is described in detail
190 in Supplementary Text S2.

191 $\text{PM}_{2.5}$ was reconstructed as the sum of organic matter ($\text{OM} = 1.6 \times \text{OC}$) (Guinot et
192 al., 2007), EC, non-dust water-soluble ions (nd-WSII, and fine mineral dust (FMD)
193 derived from crustal elements (Malm et al., 1994; Tian et al., 2023), showing good
194 agreement with measured $\text{PM}_{2.5}$ ($r = 0.82$). Here, nd-WSII was defined as the sum of
195 K^+ , NH_4^+ , NO_3^- , and SO_4^{2-} , while Na^+ , Ca^{2+} , Mg^{2+} , and Cl^- were excluded. Ca^{2+} and
196 Mg^{2+} were treated as dust-related species, Na^+ was excluded due to generally elevated

197 blanks associated with quartz-fiber filters and glassware, and Cl^- was excluded given
198 its strong association with Mg^{2+} ($r = 0.77$, Table S1). The FMD was defined as follows:

$$199 \quad [FMD] = 2.20[Al] + 2.49[Si] + 1.63[Ca] + 2.42[Fe] + 1.94[Ti] \quad (4)$$

200 where $[Si] = 1.5 [Al]$.

201 **2.2 Multiple Linear Regression**

202 The influence of particle size and chemical composition on AAE_{sfc} was assessed
203 using a standardized multiple linear regression:

$$204 \quad \widehat{\text{AAE}}_{\text{sfc}} = a + b \times \widehat{\text{FMD}} + c \times \widehat{\text{nd-WSII}} + d \times \widehat{\text{D}}_{\text{SMPS}} + e \times \widehat{\text{D}}_{\text{APS}} \quad (5)$$

205 where $\widehat{\text{AAE}}_{\text{sfc}}$ denotes the standardized AAE_{sfc} ; a represents the intercept term, any
206 remaining influence not parameterized by the selected predictors is captured by the
207 intercept term; b , c , d , and e are regression coefficients; $\widehat{\text{FMD}}$, $\widehat{\text{nd-WSII}}$, $\widehat{\text{D}}_{\text{SMPS}}$,
208 and $\widehat{\text{D}}_{\text{APS}}$ are standardized variables of FMD fraction, nd-WSII fraction, and mean
209 diameters from SMPS and APS, respectively. To ensure consistent temporal support
210 between offline chemistry and online optical measurements, we aggregate AAE_{sfc} (and
211 size-related parameters) over the same sampling windows and use these window-mean
212 values. We note that AAE_{sfc} can vary within a given sampling period; however, such
213 within-period variability is not resolvable by the integrated filter chemistry and
214 therefore cannot be explicitly attributed at finer temporal resolution. To transparently
215 characterize the associated representativeness uncertainty, we quantify the within-
216 window dispersion of AAE_{sfc} using the standard deviation across all sampling windows
217 and provide its frequency and cumulative distributions (Fig. S2). In particular, $\sim 90\%$

218 of the sampling periods show a standard deviation no greater than 0.35. This result
219 indicates that window-mean AAE_{sfc} provides a reasonable representative value at the
220 filter timescale. Due to power outage on 27 December 2023 and 3 January 2024,
221 daytime data for 27 December and both daytime and nighttime data for 3 January were
222 unavailable. In future studies, higher-time-resolution measurements of aerosol
223 chemical composition would be valuable for more directly linking short-timescale
224 composition variability with AAE.

225 Notably, to further evaluate the robustness of the regression coefficients, we
226 conducted a nonparametric bootstrap analysis with 1000 resamples. We also tested an
227 extended model including EC and OM fractions as additional predictors. However, the
228 extended model yielded highly unstable coefficient estimates under bootstrap
229 resampling, with strong dispersion and frequent sign changes (Table S1). In contrast,
230 the reduced model provides stable and physically interpretable coefficients for the key
231 predictors and demonstrates good predictive skill for AAE_{sfc} (the coefficient of
232 determination (R^2) = 0.75, root mean square error (RMSE) = 0.13, mean absolute error
233 (MAE) = 0.10; Table S2). Consistent with these robustness results, our correlation
234 analysis further indicates that EC and OM fractions are not significantly associated with
235 AAE_{sfc} during this campaign (Section 3.2). Therefore, we retained the parsimonious
236 formulation without EC and OM fractions for subsequent analyses (Equation (5)).

237 **2.3 AERONET Data**

238 We used data from the Beijing Aerosol Robotic Network (AERONET) site (39.98°

239 N, 116.38° E). Level 2.0 quality-assured Version 3 inversion products were
240 selected. Key parameters include aerosol absorption optical depth (AAOD) at 440, 675,
241 870, and 1020 nm to calculate columnar AAE (AAE_{col}):

$$242 \quad AAOD_{\lambda} = k \times \lambda^{-AAE_{col}} \quad (6)$$

243 where k is a constant. In addition, aerosol size-related parameters were obtained,
244 including volume size distributions for radii in the 0.05–15.00 μm range, mean radii of
245 fine-mode and coarse-mode particles (R_{fine} , R_{coarse}), as well as volume concentrations
246 of fine-mode (0.05–0.60 μm , vol_{fine}) (Dubovik et al., 2002) and total particles (vol_{total}).

247 The fine-mode fraction (FMF) was then calculated as:

$$248 \quad FMF = \frac{vol_{fine}}{vol_{total}} \quad (7)$$

249 To investigate the influence of chemical composition on AAE_{col} , we used the
250 chemical composition dataset derived from AERONET inversions (Zhang et al., 2024),
251 including black carbon (BC), brown carbon (BrC), coarse-mode absorbing insoluble
252 matter (CAI, representing coarse absorbing dust), coarse-mode non-absorbing insoluble
253 matter (CNAI, representing coarse non-absorbing dust and aged carbonaceous aerosols),
254 and fine-mode non-absorbing insoluble matter (FNAI, representing fine non-absorbing
255 dust and organic carbon) (Li et al., 2019; Zhang et al., 2024).

256 Notably, the column chemical components (BC, BrC, CAI, CNAI, and FNAI) used
257 here are retrieval-based and should not be interpreted as directly measured chemical
258 mas. They are inferred from spectral Sun–sky photometer observations through the
259 AERONET inversion (which retrieves column-integrated size distribution and complex

260 refractive index from AOD and sky radiances) and a subsequent component-mixing
261 framework (GRASP/Component) that maps the retrieved optical constraints to
262 optically equivalent component fractions (Dubovik et al., 2000; Sinyuk et al., 2020; Li
263 et al., 2019). In doing so, the component retrieval necessarily relies on prescribed
264 assumptions, notably fixed complex refractive indices for the dry components, an
265 internal-mixing rule (commonly Maxwell–Garnett effective medium approximation) to
266 compute effective optical properties, and constraints on how absorbing components are
267 partitioned between fine and coarse modes (Li et al., 2019). For dust, non-sphericity is
268 treated using spheroid-based scattering models rather than purely spherical Mie theory
269 (Dubovik et al., 2006).

270 These assumptions introduce additional uncertainty beyond the base AERONET
271 inversion. As background, absorption-related AERONET inversion products (e.g.,
272 SSA/AAOD) are substantially less stable at low aerosol loading; under favorable
273 loading conditions, SSA uncertainty is typically on the order of ~ 0.03 , while it increases
274 rapidly as AOD decreases (Dubovik et al., 2000; Sinyuk et al., 2020). Component
275 volume fractions inherit this sensitivity and, in addition, respond to uncertainties in
276 prescribed component optics and mixing rules. Sensitivity tests in the
277 GRASP/Component literature indicate that, for $\text{AOD}_{440} \geq 0.4$ and sufficiently non-
278 negligible component fractions, the uncertainty in retrieved BC, CAI, FNAI, and CNAI
279 volume fractions is commonly within $\sim 50\%$, whereas BrC generally remains more
280 uncertain at low BrC fractions but can approach the $\sim 50\%$ level when BrC becomes a

281 substantial contributor (Li et al., 2019). Nevertheless, this approach has been applied
 282 by Zhang et al. (2022) and Zhang et al. (2024), who obtained reliable aerosol chemical-
 283 component information from remote-sensing measurements. To reduce the low-loading
 284 regime where absorption and component retrievals are most uncertain, we restricted our
 285 analysis to $AOD_{440} > 0.4$.

286 To further assess the radiative impacts of aerosols, we also employed AERONET
 287 shortwave instantaneous aerosol direct radiative forcing (ADRF) and aerosol radiative
 288 forcing efficiency (ARFE) data, where ARFE is defined as ADRF per unit aerosol
 289 optical depth (AOD) at 550 nm, reported at the top of the atmosphere (TOA), bottom
 290 of the atmosphere (BOA), and in the atmosphere (ATM) (Holben et al., 1998). These
 291 radiative quantities are computed within the AERONET inversion radiative-transfer
 292 module under cloud-free conditions, using AERONET-retrieved aerosol optical
 293 properties and surface albedo as inputs. ADRF is defined as the difference in broadband
 294 shortwave radiative fluxes between aerosol-free and aerosol-laden conditions (García
 295 et al., 2008):

$$296 \quad ADRF_{TOA} = F_{0,TOA}^{\uparrow} - F_{TOA}^{\uparrow} \quad (8)$$

$$297 \quad ADRF_{BOA} = F_{BOA}^{\downarrow} - F_{0,BOA}^{\downarrow} \quad (9)$$

$$298 \quad ADRF_{ATM} = ADRF_{TOA} - ADRF_{BOA} \quad (10)$$

299 where F and F_0 denote radiative fluxes with and without aerosols, and arrows indicate
 300 upward or downward fluxes. ARFE is defined as radiative forcing per unit aerosol
 301 optical depth:

302
$$ARFE = \frac{ADRF}{AOD_{550}} \quad (11)$$

303 where AOD_{550} is the AOD at 550 nm. Defined this way, negative ADRF and ARFE
304 indicate shortwave cooling.

305 **2.4 Shapley Additive Explanations (SHAP)**

306 To quantify how particle size and chemical composition control the AAE_{col} , we
307 trained and compared three ensemble tree-based regressors: Extreme Gradient
308 Boosting (XGBoost), Random Forest (RF), and Categorical Boosting (CatBoost). Each
309 model was trained using seven predictor variables, including five chemical
310 compositions (BrC, BC, CAI, CNAI, and FNAI), and four size parameters (R_{fine} , R_{coarse} ,
311 vol_{fine} , and volume concentrations of coarse-mode (vol_{coarse})).

312 Model performance was evaluated using a consistent training–testing split (80%
313 of dataset were used for the training set, and 20% were used for the test set) and
314 quantified by R^2 , RMSE, and MAE. The RF model achieved an R^2 of 0.58, an RMSE
315 of 0.43, and an MAE of 0.30. In comparison, the CatBoost model yielded an R^2 of 0.64,
316 an RMSE of 0.40, and an MAE of 0.29, while the XGBoost model showed an R^2 of
317 0.64, an RMSE of 0.40, and an MAE of 0.30 (Fig. S3). The CatBoost model in our case
318 was subsequently adopted for further interpretation. Furthermore, the SHAP analysis
319 was applied to decompose the model output into additive feature contributions,
320 enabling quantitative assessment of the relative contribution and sensitivity of
321 individual aerosol composition and size parameters in predicting.

322 Similarly, to evaluate aerosol radiative impacts, XGBoost, RF, and CatBoost

323 models also were trained using distinct predictor sets for different radiative metrics.
 324 The AERONET ADRF and ARFE products are generated by a radiative-transfer
 325 calculation (Section 2.4); therefore, our goal is not to replace radiative transfer. Here
 326 machine-learning model is used to quantify the relative importance of AAE_{col} as a
 327 predictor of ADRF and ARFE variability, rather than implying a causal pathway where
 328 AAE_{col} independently drives ADRF and ARFE.

329 For ADRF, five optical properties (AOD, single scattering albedo (SSA),
 330 asymmetry parameter (g), surface albedo (SA), and AAE_{col}) were used as inputs. For
 331 ARFE, the target definition ($ARFE = ADRF/AOD$) was kept unchanged; however,
 332 AOD was included during model fitting together with SSA, g, SA, and AAE_{col} so that
 333 the models could learn any residual nonlinearity and interactions involving AOD.
 334 Performance was again evaluated using a consistent training–testing split, with 80% of
 335 the dataset used for training and the remaining 20% for testing. The evaluation was
 336 quantified by R^2 , RMSE, and MAE. The performance metrics for the three models are
 337 summarized in Fig. S4-S5. CatBoost in our case was retained as the best-performing
 338 model across TOA, BOA, and ATM, as it showed the highest or near-highest R^2 together
 339 with the lowest or near-lowest RMSE and MAE among the tested models. R^2 , RMSE,
 340 and MAE are defined as follows:

$$341 \quad R^2 = 1 - \frac{\sum_{i=1}^n (y_i - \hat{y}_i)^2}{\sum_{i=1}^n (y_i - \bar{y})^2} \quad (12)$$

$$342 \quad RMSE = \sqrt{\frac{1}{n} \sum_{i=1}^n (y_i - \hat{y}_i)^2} \quad (13)$$

343
$$MAE = \frac{1}{n} \sum_{i=1}^n |y_i - \hat{y}_i| \quad (14)$$

344 where n represents the number of input samples. y_i and \hat{y}_i are the observed and
 345 predicted values, respectively; \bar{y} refers to the mean of the target values predicted by
 346 the model. In this study, y corresponds to the target variable, including AAE_{sfc} (Section
 347 2.2), AAE_{col} , ADFR, and ARFE in this Section.

348 To attribute ARFE variations while controlling for AOD, we employed SHAP with
 349 a scenario-based conditioning approach. Specifically, we recomputed SHAP values on
 350 the held-out test set after fixing AOD to four levels (25th, 50th, 75th percentiles, and
 351 mean), computed from the training set to avoid information leakage, while leaving all
 352 other predictors unchanged. This yields SHAP attributions for SSA, g , SA, and AAE_{col}
 353 conditional on AOD at representative states. (The 50th percentile case is shown in the
 354 main text, others in Supplementary). For ADRF, SHAP was computed in the standard
 355 manner using all five predictors (AOD, SSA, g , SA, AAE) without conditioning.

356 **3 Results and Discussion**

357 **3.1 Aerosol Characteristics During the Field Campaign**

358 Figure 1 provides the near-surface AAE (AAE_{sfc}) variability and its co-variation
 359 with $PM_{2.5}$ composition and particle size during the Beijing campaign. In Fig. 1a, the
 360 stacked bars show the window-resolved $PM_{2.5}$ mass fractions of non-dust water-soluble
 361 ions (nd-WSII), fine mineral dust (FMD), organic matter (OM), and elemental carbon

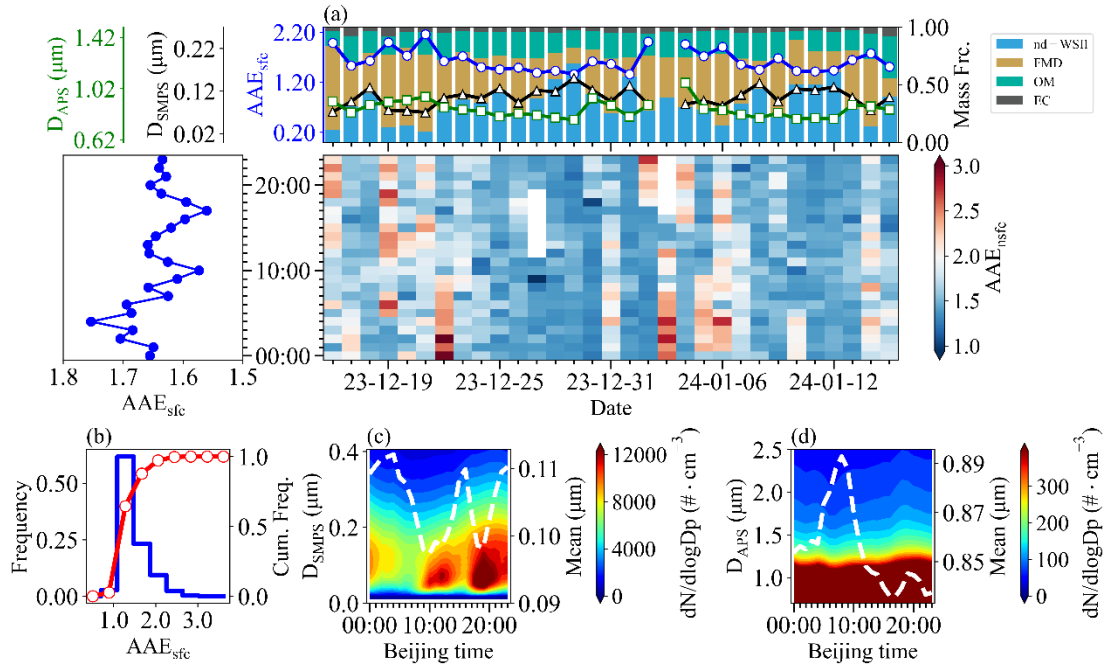
362 (EC), overlaid with AAE_{sfc} and the mean particle diameters derived from the fine-mode
363 (SMPS) and coarse-mode (APS) measurements. Notably, periods with elevated FMD
364 fractions generally coincide with higher AAE_{sfc} , whereas intervals dominated by nd-
365 WSII tend to correspond to lower AAE_{sfc} , consistent with dust-related enhancement of
366 short-wavelength absorption. These co-variations motivate the quantitative attribution
367 in Section 3.2, where we assess how the fractions of FMD and nd-WSII relate to the
368 observed spectral absorption dependence.

369 The overall distribution of AAE_{sfc} is summarized in Fig. 1b. AAE_{sfc} ranges from
370 0.90 to 3.0 and occurs most frequently between 1.10–2.0, with a mean value of
371 1.64 ± 0.32 . A pronounced high- AAE_{sfc} tail (values above 2.0) occurs episodically (Fig.
372 1b), suggesting intermittent enhancement of short-wavelength absorption. Such
373 elevated values likely resulted from winter heating emissions (Tian et al., 2019; Yan et
374 al., 2017) and mineral dust contributions (Fig. 1a), both known to raise AAE (Liu et al.,
375 2018).

376 The heat map in Fig. 1a further illustrates the time-of-day evolution of AAE_{sfc}
377 across the campaign, and the accompanying diurnal profile highlights a clear nighttime
378 enhancement relative to daytime. AAE_{sfc} showed a clear night-high and day-low pattern
379 (Fig. 1a), consistent with the evolution of particle size distributions. Fine-mode number
380 concentrations derived from SMPS increased during the morning rush hours and
381 nighttime residential activity (Fig. 1c). By contrast, coarse-mode diameters from APS
382 were larger in the early morning and decreased during the day (Fig. 1d). These results

383 demonstrate that AAE_{sfc} was co-regulated by both composition and size, providing the
384 observational evidence for the subsequent machine-learning analysis to quantify their
385 relative contributions and radiative implications.

386 Figure S6 further shows the multi-wavelength absorption coefficients and their
387 diurnal behavior. Aerosol absorption coefficients exhibit a clear spectral decrease from
388 the near-UV to the near-IR, with mean values of 13.19 ± 9.91 , 6.80 ± 6.15 , and $3.77 \pm$
389 3.27 Mm^{-1} at 375, 532, and 870 nm, respectively (mean \pm one standard deviation) (Fig.
390 S6). The corresponding mass absorption efficiencies are relatively low (0.49 ± 0.24 ,
391 0.21 ± 0.08 , and $0.12 \pm 0.04 \text{ m}^2 \cdot \text{g}^{-1}$), reflecting the dominance of nd-WSII, which
392 accounted for 42.9% of $PM_{2.5}$ mass (Fig. 1a). Absorption coefficients at three
393 wavelengths are consistently higher absorption at night and a peak around 23:00 (Fig.
394 S6), driven by reduced tropospheric boundary layer height, lower afternoon
395 temperatures and wind speeds (Fig. S7), and enhanced emissions from nighttime traffic
396 and heating (Guo et al., 2016; Zhao et al., 2019).



397

398 **Figure 1. Aerosol absorption characteristics during the campaign.** (a) Time series
 399 of mean particle diameters derived from SMPS and APS, mass fractions of organic
 400 matter (OM), elemental carbon (EC), non-dust water-soluble inorganic ions (nd-WSII),
 401 and fine mineral dust (FMD), together with daily averaged near-surface AAE (AAE_{sfc}).
 402 (b) Frequency distribution of AAE_{sfc} . (c–d) Diurnal variations of aerosol particle
 403 number size distributions from SMPS (c) and APS (d).

404 3.2 Influence of Composition and Size on Near-surface AAE

405 The EC mass fraction shows no correlation with AAE_{sfc} ($r = 0.09$, $p = 0.49$; Fig.
 406 2a). This is plausible because EC is an operational thermal fraction and does not directly
 407 represent the optically effective BC absorption, which can be substantially modified by
 408 mixing state and coating (Petzold et al., 2013). Similarly, the OM mass fraction is not
 409 significantly correlated with AAE_{sfc} ($r = -0.11$, $p = 0.40$; Fig. 2a). In contrast to study
 410 dominated by biomass burning, where light-absorbing organic carbon can account for >

411 50% of the mass fraction and strongly enhance AAE (Wang et al., 2021). During the
412 Beijing campaign, however, OM contributes only ~19% of total PM_{2.5} mass and BrC
413 fractions therefore are relatively low. Although BrC exhibits intrinsically high AAE
414 values (Laskin et al., 2015; Moosmüller et al., 2011), its impact is diminished in the
415 mixed aerosol matrix due to the influence of other dominant compositions.

416 We observed a statistically significant negative correlation between AAE_{sfc} and
417 carbonaceous aerosol AAE (AAE_{CA}) (Fig. 2b), indicating that the non-carbonaceous
418 aerosol had a significantly stronger role in shaping the absorption spectral dependence
419 under complex pollution conditions. Due to nitrogen dioxide (NO₂) concentrations were
420 elevated at night (Fig. S8), which can interfere with PAX instruments, particularly at
421 shorter wavelengths (Arnott et al., 2000; Gyawali et al., 2012). Therefore, we restrict
422 the analysis here to daytime data (Fig S9). This pattern therefore cannot be ascribed
423 simply to inter-instrument discrepancies.

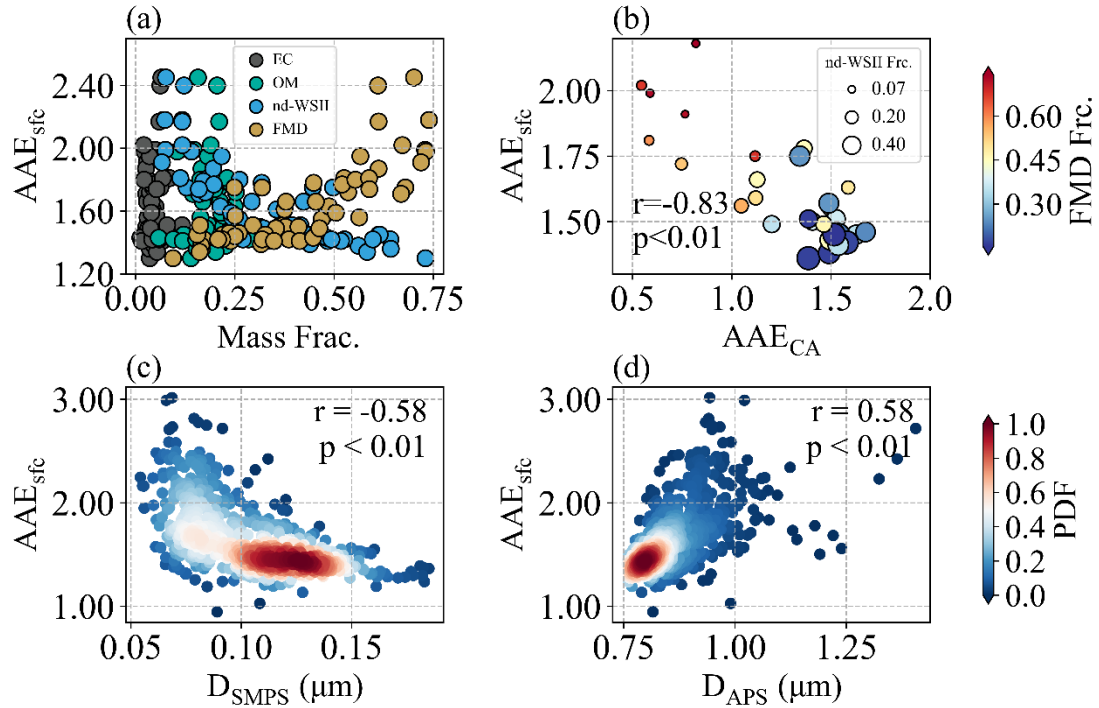
424 AAE_{sfc} exhibits a significant positive correlation with the mass fraction of FMD
425 ($r = 0.79$, $p < 0.01$) and a negative correlation with nd-WSII ($r = -0.78$, $p < 0.01$) (Fig.
426 2a). The AAE_{sfc} enhancement associated with FMD can be attributed to metal oxides
427 such as hematite and goethite, which strongly absorb in the UV wavelengths and
428 steepen the spectral dependence (Bi et al., 2016). By contrast, nd-WSII (mostly sulfates,
429 nitrates, and ammonium particles) primarily behaves as a weakly absorbing (nearly
430 scattering-only) component in the visible–near-infrared (Seinfeld & Pandis, 2016), and
431 an increase in its mass fraction therefore tends to dilute the contribution of absorbing

432 species to total $\text{PM}_{2.5}$ absorption. In our surface dataset, this dilution effect is expected
433 to reduce the relative importance of short-wavelength absorbers and, in turn, weaken
434 the apparent wavelength dependence of bulk absorption, leading to lower AAE_{sfc} when
435 nd-WSII dominates. We note that a “lensing effect” associated with non-absorbing
436 coatings has been reported to enhance AAE_{CA} (Cappa et al., 2012; Zhang et al., 2025).
437 However, the carbonaceous components contributed only a small fraction of $\text{PM}_{2.5}$ mass
438 during our campaign. Consequently, any potential lensing-related enhancement was
439 likely too small relative to the total aerosol and variability to yield a detectable positive
440 correlation between AAE_{sfc} and the nd-WSII mass fraction. In this regime, nd-WSII is
441 better interpreted as a marker of secondary inorganic aerosol loading that mainly
442 increases scattering and dilutes absorber fractions.

443 Particle size also plays a critical role. AAE_{sfc} is negatively associated with the fine-
444 mode mean diameter from SMPS (D_{SMPS} , $r = -0.58$; Fig. 2c) and positively associated
445 with the coarse-mode mean diameter from APS (D_{APS} , $r = 0.58$; Fig. 2d). Here, the
446 correlation analysis is used as an exploratory step to describe these first-order
447 relationships, whereas the standardized multiple linear regression (MLR) estimates the
448 multivariate associations after accounting for predictor covariation. Consistent with the
449 bivariate results, the MLR yields a negative standardized coefficient for D_{SMPS} (-0.02)
450 and a positive coefficient for D_{APS} (0.44), confirming that the coarse-mode size metric
451 provides the stronger size-related contribution in the multivariate setting.

452 The composition terms show a similarly coherent pattern across the two analyses.

453 FMD is positively associated with AAE_{sfc} in the bivariate correlations and remains
454 positive in the MLR (0.35), whereas nd-WSII shows a negative association and remains
455 negative in the MLR (-0.16). Importantly, particle size and composition are not
456 independent in this winter dataset. Periods with larger coarse-mode diameters tend to
457 coincide with enhanced fine mineral dust fraction ($r=0.64$; Fig. S10), consistent with
458 stronger dust influence. Conversely, periods characterized by smaller fine-mode
459 diameters are associated with elevated nd-WSII fraction ($r=0.89$; Fig. S10), consistent
460 with secondary inorganic build-up and hygroscopic growth that increase scattering and
461 dilute the relative contribution of absorbing components. Together, these results
462 indicate that higher AAE_{sfc} is associated with a regime of larger particles and stronger
463 dust contribution, whereas lower AAE_{sfc} occurs when secondary inorganic matter is
464 more influential and dust contributions are reduced. Overall, AAE_{sfc} is influenced not
465 only by carbonaceous aerosols, but also strongly by other chemical components,
466 particularly mineral dust-related particles, non-dust water-soluble inorganic ions, and
467 particle-size distributions.



468

469 **Figure 2. Relationships of near-surface absorption Ångström exponent (AAE_{sfc})**

470 **with chemical composition and particle size. (a) Scatter plots of chemical mass**

471 **concentration fraction and total aerosol AAE_{sfc} . (b) Relationship between AAE_{sfc} and**

472 **carbonaceous aerosol AAE (AAE_{CA}), with symbol size representing the non-dust**

473 **water-soluble ions (nd-WSII) fraction and color denoting the fine mineral dust (FMD)**

474 **fraction. (c–d) Correlations of AAE_{sfc} with mean particle diameters derived from SMPS**

475 **(c) and APS (d), respectively. Shaded colors indicate probability density.**

476 **3.3 Quantitative Contributions of Composition and Size to Columnar AAE**

477 The relationships between mass fractions of chemical composition and AAE_{col}

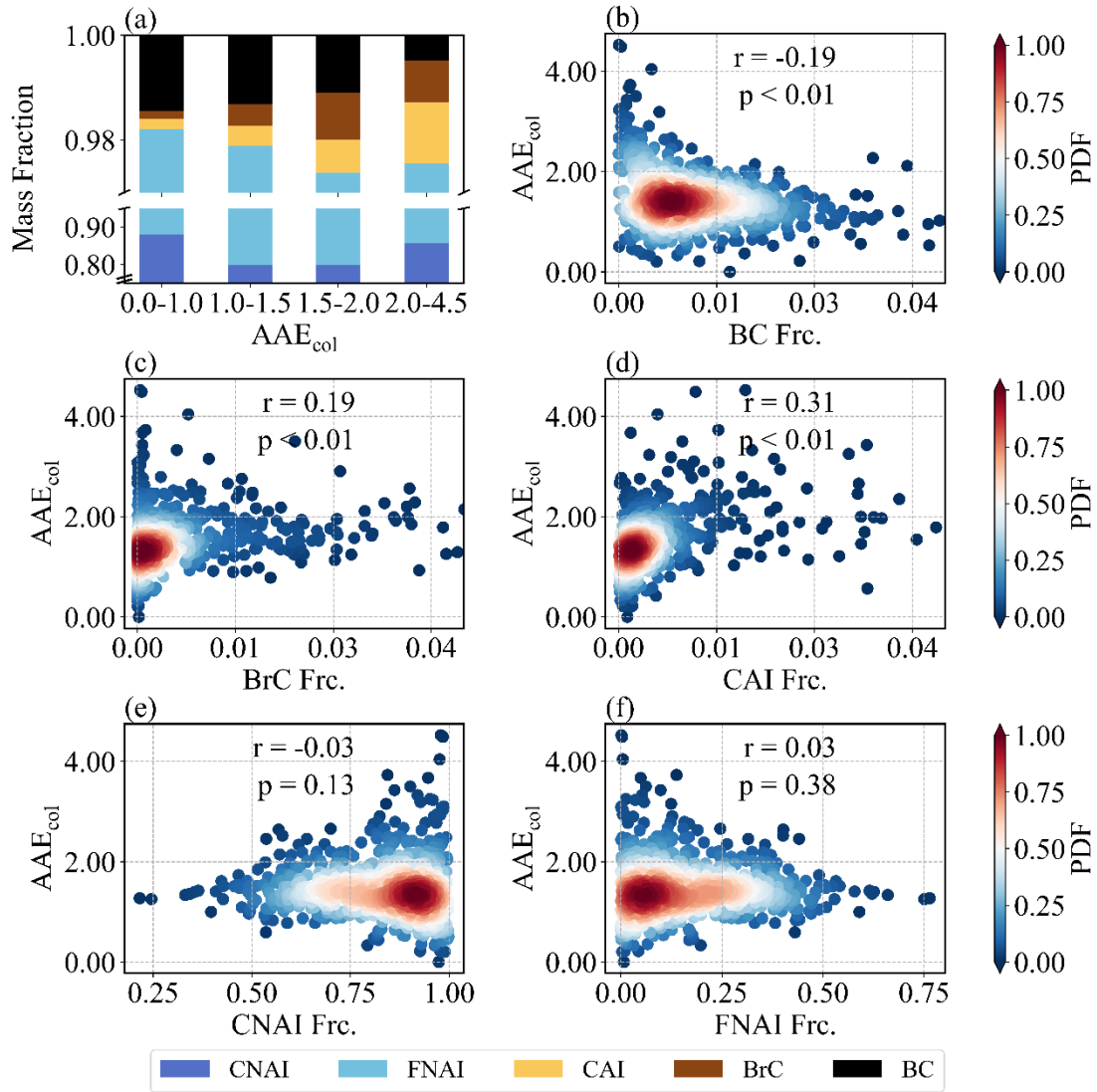
478 were studied using AERONET data (Fig. 3). The CNAI and FNAI mass fractions varied

479 little and exhibited no significant correlations with AAE_{col} ($r = -0.03$ and 0.03 , $p > 0.1$),

480 indicating a negligible role in setting the absorption spectral dependence. In contrast,

481 BC, BrC, and CAI displayed clear associations. Higher AAE_{col} (>1.5) were associated
482 with marked increases in BrC and CAI, whereas lower AAE_{col} (<1.5) corresponded to
483 relatively higher BC contributions. Correlation analysis is consistent with these patterns:
484 AAE_{col} was negatively correlated with BC ($r = -0.19$, $p < 0.01$), in line with its weak
485 wavelength dependence, but positively correlated with BrC ($r = 0.19$, $p < 0.01$) and CAI
486 ($r = 0.31$, $p < 0.01$), underscoring the strong wavelength dependence of BrC and dust.
487 These findings were similarly to our surface campaign, particularly regarding dust's
488 amplifying effect on AAE_{col} .

489 The impacts of aerosol size distribution on AAE_{col} were clearly reflected (Fig. 4).
490 With AAE_{col} increasing, the peaks of both fine and coarse modes shifted to smaller sizes
491 (Fig. 4a), indicating an overall refinement of the size distribution. The R_{fine} and R_{coarse}
492 were both negatively correlated with AAE_{col} ($r = -0.27$ and -0.26 , $p < 0.01$; Fig. 4c,
493 4d), demonstrating that reductions in particle size in both modes enhanced the spectral
494 dependence. Interestingly, FMF decreased with increasing AAE_{col} (Fig. 4b), suggesting
495 that coarse-mode particles retained a substantial volumetric contribution even under
496 high AAE_{col} conditions.



497

498 **Figure 3. Relationships between columnar absorption Ångström exponent (AAE_{col})**

499 **and major aerosol chemical compositions. (a) Mass fractions of fine-mode non-**

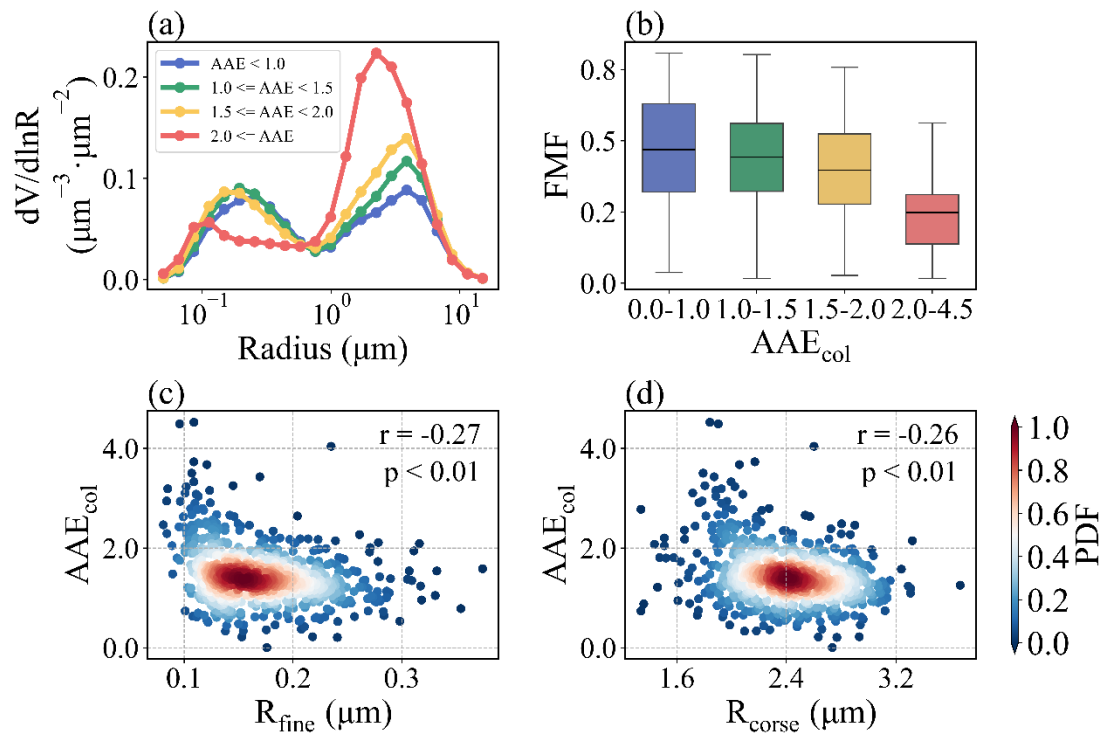
500 **absorbing soluble matter (FNAI), coarse-mode non-absorbing soluble matter (CNAI),**

501 **coarse-mode absorbing soluble matter (CAI, representing dust), brown carbon (BrC),**

502 **and black carbon (BC) across different AAE_{col} bins. (b-f) Correlations between AAE_{col}**

503 **and the mass fractions of BC, BrC, CAI, CNAI, and FNAI, respectively; shaded colors**

504 **denote probability density.**



505

506 **Figure 4. Relationships between columnar absorption Ångström exponent (AAE**

507 **col) and aerosol size distribution characteristics. (a) Volume size distributions**

508 **grouped by AAE_{col} bins. (b) Fine-mode fraction (FMF) by AAE_{col} bins, with horizontal**

509 **lines indicating means. (c–d) Correlations of AAE_{col} with effective radius of fine-mode**

510 **(R_{fine}) and coarse-mode (R_{coarse}) particles, respectively.**

511 Machine learning analysis further quantified relative contributions, as illustrated

512 in Fig. 5a. It is found that showed that CAI had the strongest explanatory power,

513 accounting for ~19% of the model's predictive power, confirming the dominant role of

514 dust in amplifying spectral absorption. BrC was second (18.5%) and BC was third

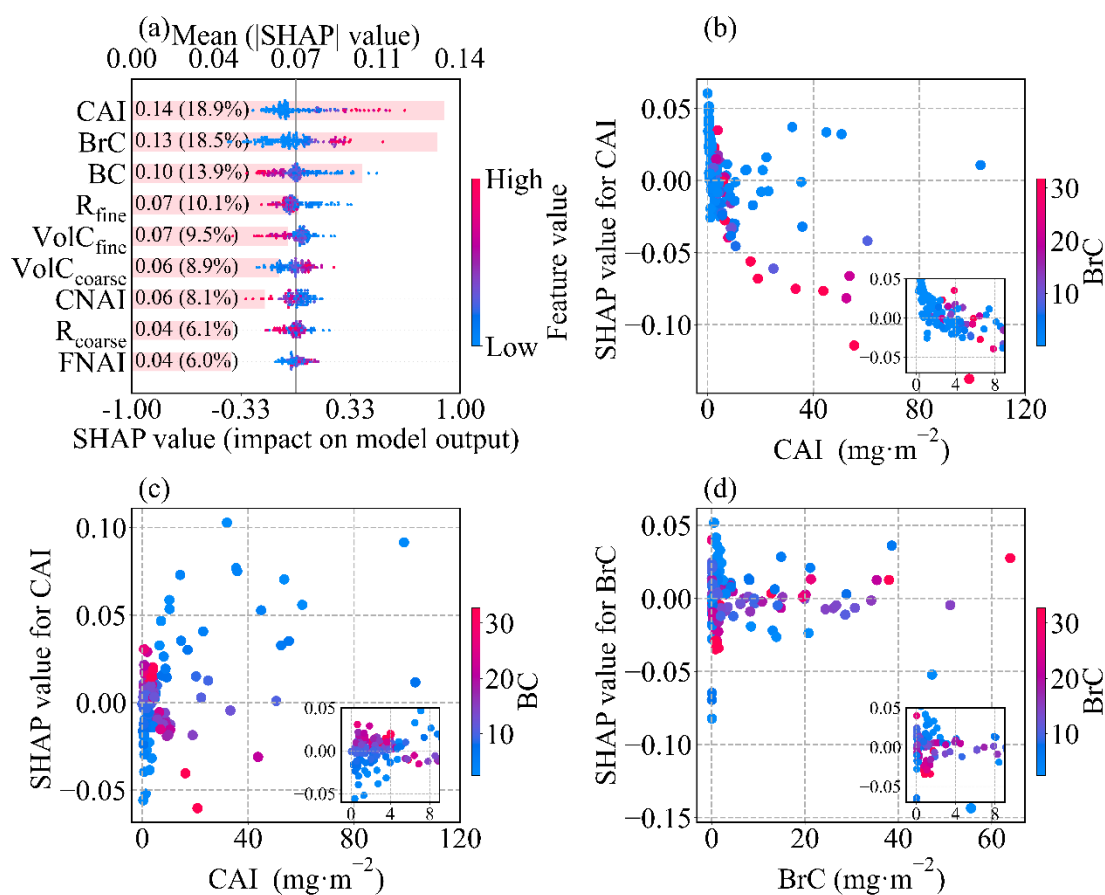
515 (13.9%), together with CAI explaining ~50% of model's predictive power (as measured

516 by mean absolute SHAP value). Among the size-related predictors, R_{fine} alone

517 accounted for about one quarter (~29%) of the cumulative importance of all size metrics,

518 making it the most influential size parameter. In addition, its importance was also

519 clearly higher than CNAI and FNAI (Fig. 5a). During the prediction process, it is
 520 observed that higher values of BrC, CAI, and volume concentrations of coare-mode
 521 ($\text{vol}_{\text{coarse}}$) corresponded to higher SHAP values and higher values of other predictors
 522 corresponded to smaller SHAP values (Fig. 5a). These responses are fully consistent
 523 with the correlations between AAE_{col} and these parameters (Fig. 3b–d; Fig. 4c–d).



524

525 **Figure 5. SHAP interpretation of the machine-learning model for columnar AAE.**

526 (a) Attribution of chemical compositions and particle size parameters to columnar AAE.

527 Each horizontal bar represents the mean absolute SHAP value of a feature, indicating

528 its overall impact on the model output; the color gradient shows the effect of feature

529 values on columnar AAE, with red indicating a positive influence and blue indicating a

530 negative influence. Features are ranked by importance. (b–c) SHAP dependence plots

531 corresponding to CAI. (d) SHAP dependence plots corresponding to BrC.

532 To connect these statistical attributions to physically plausible behavior, we
533 performed a simple Mie-theory sensitivity analysis (Text S3; Fig. S11). First, we varied
534 the imaginary part of the refractive index at 440 nm (k_{440}) while keeping the size
535 distribution fixed. Second, keeping refractive index fixed and shifting the fine- and
536 coarse-mode radii to 80%, 90%, 100%, 110%, and 120% of their baseline values (with
537 mode-integrated volume conserved).

538 Varying k_{440} produces a substantially larger change in the modeled AAE_{col} than the
539 size-shift experiments (Fig. S12), indicating that changes in short-wavelength
540 absorptivity exert stronger leverage on AAE than variations in modal radii. Because we
541 altered k_{440} while keeping k_{870} unchanged, this experiment specifically isolates
542 enhanced absorption in the short wavelengths which is consistent with increased
543 contributions from aerosols that preferentially absorb at shorter wavelengths, such as
544 absorbing mineral dust and brown carbon (Russell et al., 2010). Spectral refractive
545 indices retrieved by AERONET are known to vary systematically across aerosol types
546 and can be used to infer absorbing components, supporting the interpretation of k as a
547 proxy for composition-related absorption variability (Dubovik et al., 2002; Wang et al.,
548 2013). Fine-mode shifts produce a clearer change in the AAE_{col} than coarse-mode shifts
549 (Fig. S12b, S12c), consistent with R_{fine} being the leading size predictor in Fig. 5a. Taken
550 together, the SHAP results and the Mie sensitivity tests support a consistent
551 interpretation that AAE_{col} is not influenced by BC or BrC alone; it is primarily

552 associated with dust and secondarily by particle-size structure (size metrics together
553 ~35%) (Fig. 5a), underscoring the need to account for both composition and size when
554 evaluating spectral absorption.

555 To further investigate the interaction effects of major parameters on AAE_{col}
556 prediction, we selected CAI, BrC, and BC, the three most influential predictors by
557 SHAP, to analyze their interactions (Fig. 5b-5f). When CAI loading was below 10
558 $mg \cdot m^{-2}$, BrC suppressed the positive impact of CAI loading and progressively drove it
559 toward a negative contribution. When CAI loading exceeded 10 $mg \cdot m^{-2}$, lower BrC is
560 more likely than higher BrC to sustain or enhance the positive marginal effect of CAI,
561 although the magnitude is weaker than in the CAI loading $< 10 mg \cdot m^{-2}$ regime. For
562 CAI loading in the range 0–4, higher BC yielded a positive marginal effect of CAI on
563 AAE_{col} , whereas lower BC yielded a negative one. Once CAI loading is greater than 4
564 $mg \cdot m^{-2}$, this relationship reverses, with higher BC more likely to make further increases
565 in CAI contribute negatively to AAE_{col} . As BrC increases, BC progressively reduces
566 the positive and negative contributions of BrC to AAE_{col} . These interactions indicate
567 that models of aerosol spectral absorption should explicitly represent the mutual
568 constraints among CAI, BrC, and BC to better identify and quantify AAE drivers.

569 **3.4 The comparison between surface and columnar AAE.**

570 Sections 3.2 and 3.3 provide two complementary perspectives on AAE. The near-
571 surface campaign (December 2023–January 2024) represents a specific winter
572 pollution regime, whereas the AERONET analysis provides a longer-term perspective

573 (2001–2019). Despite these differences, the two analyses converge on a consistent
574 mechanistic interpretation. AAE increases when short-wavelength absorption becomes
575 relatively stronger, and dust-related absorption plays a central role in influencing this
576 spectral dependence. In the surface analysis, the fine mineral dust fraction within $PM_{2.5}$
577 is significantly associated with elevated AAE_{sfc} (Fig. 2a). In the column analysis, the
578 absorbing dust component (CAI), which includes substantial coarse-mode
579 contributions (radius about 0.6–15 μm), likewise ranks among the most informative
580 predictors for AAE_{col} (Fig. 5a). Despite the different size ranges and vertical weighting,
581 both indicators consistently support the interpretation that dust-related enhancement of
582 short-wavelength absorption, and is linked to higher AAE.

583 It is also worth noting that the AAE_{col} (1.47 ± 0.56) was found to be lower than
584 that derived from the surface field campaign (Fig. 1), but this difference should not be
585 interpreted as a comparison between column and surface values. The two quantities
586 differ in both temporal representativeness (multi-year climatology versus a one-month
587 winter campaign) and measurement definition (AAOD-based column integration
588 versus near-surface absorption coefficients), so their absolute magnitudes are expected
589 to vary with aerosol regime, meteorology, and the contribution of elevated layers.
590 Therefore, our emphasis is on the consistency of predicting factors and mechanisms,
591 rather than a direct comparison of mean values.

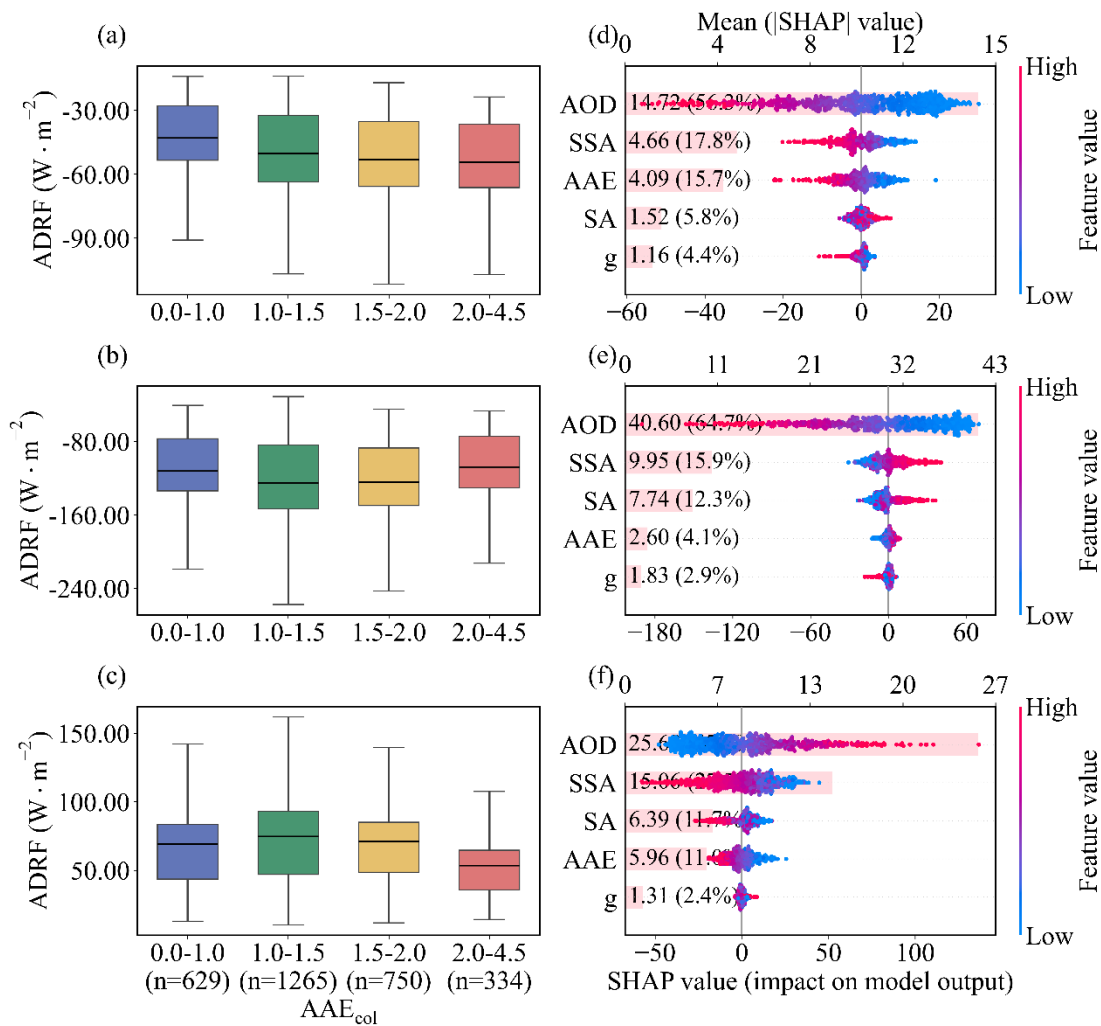
592 Finally, the two datasets complement each other in terms of strengths and
593 limitations. The surface measurements provide chemically explicit constraints but are

594 restricted to $PM_{2.5}$, thereby under-representing coarse-mode dust and any elevated-layer
595 contributions. The AERONET analysis offers direct links to radiative quantities, but its
596 component variables are retrieval-based optical constructs that depend on prescribed
597 optics and mixing assumptions (Dubovik et al., 2000; Sinyuk et al., 2020; Li et al.,
598 2019). As a result, several categories are not directly interchangeable (e.g., surface nd-
599 WSII versus retrieved non-absorbing components, surface OM versus optically defined
600 BrC, and thermal EC versus optically defined BC). Taken together, the surface
601 campaign provides process-level chemical context for short-term variability, while the
602 AERONET record generalizes the interpretation across regimes and links AAE to
603 column radiative effects with dust-related absorption emerging as the clearest cross-
604 scale consistency.

605 **3.5 The Diagnostic Power of Columnar AAE for Radiative Forcing and Efficiency** 606 **in Beijing**

607 Joint analysis of the boxplots and SHAP diagnostics revealed a robust, layer-
608 dependent correlation between the AAE_{col} and ADRF. As AAE_{col} increases from 0–1 to
609 2–4.5, cooling at the TOA intensifies, atmospheric heating weakens, and cooling at the
610 BOA is alleviated (Fig. 6a-6c). This pattern is consistent with a shift from more BC-
611 like absorption toward regimes with stronger short-wavelength absorption signatures
612 and higher scattering fractions, commonly associated with mixtures involving BrC and
613 mineral dust. SHAP method confirm that AAE_{col} is the third strongest predictor (~16%)
614 after AOD (~56%), and comparably to SSA (~18%) at TOA and consistently shifts

615 ADRF toward more negative values (Fig. 6d). At BOA, AAE_{col} explains only ~4% of
 616 the model importance. BOA cooling is primarily explained by AOD (~65.0%) and SSA
 617 (~16 %) (Fig. 6e). In the ATM, AOD and SSA remain the leading predictors, while
 618 AAE_{col} still shows importance comparable to surface albedo (SA) (both ~12%) (Fig.
 619 6f). Mechanistically, higher AAE_{col} is commonly associated with BrC and dust, which
 620 exhibit higher SSA but lower mass absorption efficiencies (MAE), thereby enhancing
 621 backscattering and solar escape (more negative TOA forcing), reducing absorption
 622 (weaker atmospheric heating), and producing a net transmission effect that mitigates
 623 BOA cooling.



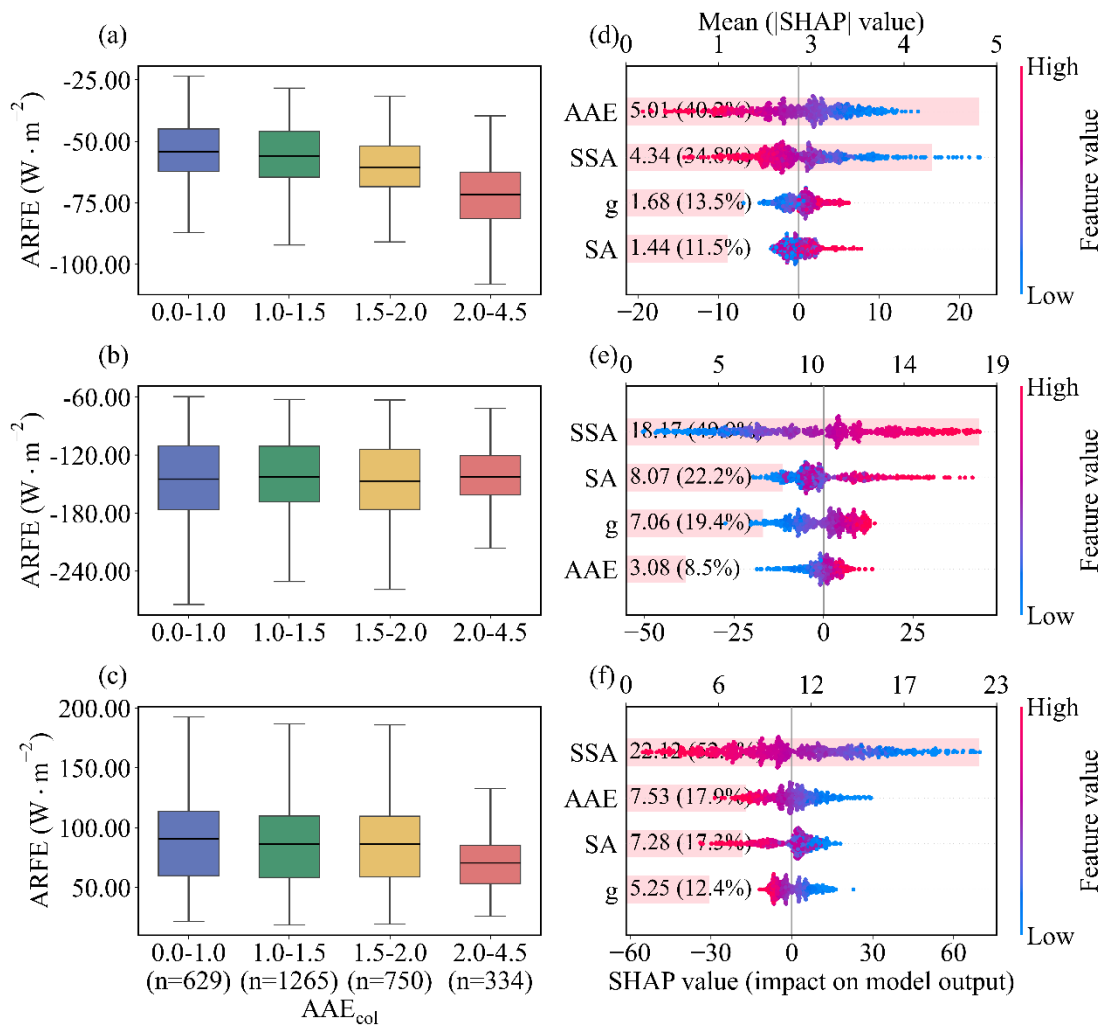
624

625 **Figure 6.** The relationship between columnar AAE (AAE_{col}) and aerosol direct
626 radiative forcing (ADRF). (a–c) Box plots of ADRF at the top of the atmosphere (a),
627 bottom (b), and in the atmosphere (c) as a function of AAE_{col} . The sample sizes for the
628 AAE_{col} bins 0.0–1.0, 1.0–1.5, 1.5–2.0, and 2.0–4.5 are $n = 629, 1265, 750,$ and 334,
629 respectively, and are identical for panels (a)–(c). (d–f) SHAP analysis quantifies the
630 relative contributions of aerosol optical depth (AOD), single scattering albedo (SSA),
631 asymmetry parameter (g), surface albedo (SA) and AAE_{col} in predicting ADRF
632 variations at the top of the atmosphere (d), at the bottom of the atmosphere (e), and in
633 the atmosphere (f). The mean absolute SHAP values (numbers in parentheses) indicate
634 the relative contribution of each predictor to the model output.

635 To better show columnar AAE's impact on ADRF, we introduce the ARFE, which
636 removes the scaling by aerosol loading and highlights intrinsic optical controls. At TOA,
637 AAE_{col} serves as a key diagnostic of cooling efficiency in the model, with mean |SHAP|
638 reaching ~40.0%, exceeding the asymmetry factor (g), SSA, and SA even when AOD
639 was conditioned at 25th (Fig. S12), 50th (Fig. 7), 75th percentiles (Fig. S13), or mean
640 (Fig. S14). Larger AAE_{col} is associated with more negative TOA ARFE (Fig. 7d),
641 indicating that, for comparable loading, regimes with steeper absorption spectra tend to
642 exhibit stronger TOA cooling efficiency.

643 At BOA, ARFE is predicted primarily by SSA (~50%), followed by g and SA,
644 with AAE_{col} predicting more modestly (~8%) (Fig. 7e). In this layer, higher SSA and
645 larger g tend to make ARFE less negative, consistent with reduced absorption and more

646 forward-directed scattering leading to greater transmittance for a fixed AOD. In the
 647 ATM, SSA is the dominant predictor of the heating-efficiency (>50%), with AAE_{col}
 648 and SA providing secondary information (both ~17%), while g plays a minor role (Fig.
 649 7f).



650
 651 **Figure 7.** The relationship between columnar AAE (AAE_{col}) and aerosol radiative
 652 forcing efficiency (ARFE). (a–c) Box plots of ARFE at the top of the atmosphere (a),
 653 bottom (b), and in the atmosphere (c) as a function of AAE_{col} . The sample sizes for the
 654 AAE_{col} bins 0.0–1.0, 1.0–1.5, 1.5–2.0, and 2.0–4.5 are $n = 629, 1265, 750,$ and $334,$
 655 respectively, and are identical for panels (a)–(c). (d–f) SHAP analysis with AOD fixed

656 at its median (50th percentile) quantifies the relative contributions of single scattering
657 albedo (SSA), asymmetry parameter (g), surface albedo (SA) and AAE_{col} in predicting
658 ARFE variations at the top of the atmosphere (d), bottom (e), and in the atmosphere (f).
659 The mean absolute SHAP values (numbers in parentheses) indicate the relative
660 contribution of each predictor to the model output.

661 Higher AAE_{col} is linked to lower atmospheric heating efficiency, reflecting a shift
662 toward aerosol types with weaker mass absorption than BC, and higher SSA further
663 suppresses in-column absorption. Overall, these results do not imply that AAE_{col} is a
664 causal driver of radiative forcing and radiative forcing efficiency; rather, AAE_{col} acts
665 as a compact descriptor of absorption spectral shape that co-varies with underlying
666 composition and size regimes. The strong association between radiative forcing and
667 ARFE therefore suggests that constraining AAE can meaningfully improve estimates
668 of forcing efficiency in radiative assessments.

669 **4 Conclusions**

670 LAAs exert a strong influence on the Earth's radiation budget, yet the spectral
671 dependence of their absorption, commonly summarized by the AAE, remains poorly
672 constrained in urban regions. Here we combined a winter in situ observation in Beijing
673 with a long-term AERONET column data (2001–2019) and an interpretable machine-
674 learning framework to quantify how composition and particle size influence AAE and
675 to evaluate what AAE implies for radiative effects.

676 Near the surface in wintertime Beijing, AAE variability co-varied primarily with
677 enhanced fractions of fine mineral dust and water-soluble inorganic ions, underscoring
678 that non-carbonaceous species can substantially modulate local absorption spectra in
679 addition to BC and BrC. At the column level, SHAP diagnostics identified CAI is the
680 most informative predictor of columnar AAE, followed by BrC and BC. Among particle
681 size metrics, the fine-mode effective radius is the leading size-related predictor and
682 accounts for about 29% of the cumulative importance of all size parameters, whereas
683 non-absorbing composition (coarse and fine non-absorbing dust and non-absorbing
684 carbonaceous aerosols) played only a minor role. Because this study is based on Beijing
685 observations, the identified predictor importance reflects a polluted urban environment
686 influenced by both anthropogenic aerosol and episodic dust. In cleaner regions the
687 relationships may weaken due to lower absorption signal, whereas in more dust-
688 influenced regions the role of dust-related predictors would likely become even stronger.
689 Although this study demonstrates the importance of bulk composition and size-
690 distribution parameters in controlling AAE, the optical properties of light-absorbing
691 aerosols can also be modulated by particle-level microphysical characteristics. For
692 example, BC morphology, from fractal to compact aggregates, and mixing state,
693 including coating thickness, coating uniformity, and the spatial distribution of
694 inclusions, may influence AAE and subsequent radiative forcing estimates (Luo et al.,
695 2023, 2024, 2025). These effects are not fully captured by bulk properties alone and
696 may contribute to the remaining uncertainty.

697 For radiative impacts, our results highlight the diagnostic value of columnar AAE
698 rather than implying a causal control. In the model trained on AERONET radiative
699 products, columnar AAE is among the most informative predictors for TOA ADRF
700 (~16%, comparable to SSA) and becomes the leading predictor for TOA ARFE (~40%),
701 with higher columnar AAE associated with more efficient TOA cooling under loading-
702 controlled conditions. By contrast, columnar AAE contributes much less to the
703 prediction of ATM and BOA ADRF and ARFE, where AOD and SSA remain the
704 primary predictors.

705 Overall, the findings of our study demonstrate the multifactorial influences of AAE
706 by composition and size and highlight its strong correlation with the vertical
707 partitioning of radiative forcing, especially at the TOA. Consequently, accurately
708 constraining AAE is essential for a realistic representation of aerosol radiation
709 interactions in regional and global models.

710 **Data and code availability**

711 The data that support the findings of this study are available in the Zenodo data
712 repository (<https://doi.org/10.5281/zenodo.17852818>, Wang et al., 2025b). The
713 AERONET data is freely available on the AERONET website
714 (<https://aeronet.gsfc.nasa.gov/>). The aerosol chemical composition derived from
715 AERONET inversion data is available from [https://doi.org/10.1175/BAMS-D-23-](https://doi.org/10.1175/BAMS-D-23-0260.1)
716 0260.1. The code scripts are also available in the Zenodo data repository

717 (<https://doi.org/10.5281/zenodo.17852818>, Wang et al., 2025b).

718 **Acknowledgments**

719 We thank the AERONET PI at the Beijing site for their efforts in establishing and
720 maintaining the site. We are also grateful to Prof. Yunfei Wu for providing access to the
721 experimental facilities at the Institute of Atmospheric Physics, Chinese Academy of
722 Sciences. We also thank the Lanzhou University Supercomputing Center for providing
723 computational support.

724 **Financial supports**

725 This research was supported by the National Natural Science Foundation of China
726 (42475080), the Gansu Province Graduate Innovation Funding Project (2025CXZX-
727 177) and the Fundamental Research Funds for the Central Universities (lzujbky-2024-
728 ey04).

729 **Author contribution**

730 PT designed the study. PT and WW received the funding. WW, PT, SZ, ZY and
731 MC analyzed the data and led the writing. WW, YZ, YW and PT conducted the field
732 campaign. WW, PT, SZ, YZ, ZY, CC, YW, MC and LZ contributed to discussion, review,
733 and edit the manuscript.

734 **Competing interests**

735 The authors declare that they have no conflict of interest.

736 **References**

737 Ångström, A.: On the Atmospheric Transmission of Sun Radiation and on Dust in the

738 Air, *Geografiska Annaler*, 11, 156–166,

739 <https://doi.org/10.1080/20014422.1929.11880498>, 1929.

740 Arnott, W. P., Moosmüller, H., and Walker, J. W.: Nitrogen dioxide and kerosene-flame

741 soot calibration of photoacoustic instruments for measurement of light absorption

742 by aerosols, *Review of Scientific Instruments*, 71, 4545–4552,

743 <https://doi.org/10.1063/1.1322585>, 2000.

744 Bahadur, R., Praveen, P. S., Xu, Y., and Ramanathan, V.: Solar absorption by elemental

745 and brown carbon determined from spectral observations, *Proc. Natl. Acad. Sci.*

746 U.S.A., 109, 17366–17371, <https://doi.org/10.1073/pnas.1205910109>, 2012.

747 Bergstrom, R. W., Pilewskie, P., Russell, P. B., Redemann, J., Bond, T. C., Quinn, P. K.,

748 and Sierau, B.: Spectral absorption properties of atmospheric aerosols, *Atmos.*

749 *Chem. Phys.*, 7, 5937–5943, <https://doi.org/10.5194/acp-7-5937-2007>, 2007.

750 Bi, J., Huang, J., Holben, B., and Zhang, G.: Comparison of key absorption and optical

751 properties between pure and transported anthropogenic dust over East and Central

752 Asia, *Atmos. Chem. Phys.*, 16, 15501–15516, <https://doi.org/10.5194/acp-16->

753 15501-2016, 2016.

754 Cappa, C., Kotamarthi, R., Selacek, A., Flynn, C., Lewis, E., McComiskey, A., and
755 Riemer, N.: Absorbing Aerosols Workshop Report, January 20–21, 2016,
756 <https://doi.org/10.2172/1471231>, 2016.

757 Cappa, C. D., Onasch, T. B., Massoli, P., Worsnop, D. R., Bates, T. S., Cross, E. S.,
758 Davidovits, P., Hakala, J., Hayden, K. L., Jobson, B. T., Kolesar, K. R., Lack, D.
759 A., Lerner, B. M., Li, S.-M., Mellon, D., Nuaaman, I., Olfert, J. S., Petäjä, T.,
760 Quinn, P. K., Song, C., Subramanian, R., Williams, E. J., and Zaveri, R. A.:
761 Radiative Absorption Enhancements Due to the Mixing State of Atmospheric
762 Black Carbon, *Science*, 337, 1078–1081, <https://doi.org/10.1126/science.1223447>,
763 2012.

764 Cazorla, A., Bahadur, R., Suski, K. J., Cahill, J. F., Chand, D., Schmid, B., Ramanathan,
765 V., and Prather, K. A.: Relating aerosol absorption due to soot, organic carbon, and
766 dust to emission sources determined from in-situ chemical measurements, *Atmos.*
767 *Chem. Phys.*, 13, 9337–9350, <https://doi.org/10.5194/acp-13-9337-2013>, 2013.

768 Chakrabarty, R. K., Arnold, I. J., Francisco, D. M., Hatchett, B., Hosseinpour, F., Loria,
769 M., Pokharel, A., and Woody, B. M.: Black and brown carbon fractal aggregates
770 from combustion of two fuels widely used in Asian rituals, *Journal of Quantitative*
771 *Spectroscopy and Radiative Transfer*, 122, 25–30,
772 <https://doi.org/10.1016/j.jqsrt.2012.12.011>, 2013.

773 Chow, J. C., Watson, J. G., Chen, L.-W. A., Chang, M. C. O., Robinson, N. F., Trimble,

774 D., and Kohl, S.: The IMPROVE_A Temperature Protocol for Thermal/Optical
775 Carbon Analysis: Maintaining Consistency with a Long-Term Database, Journal
776 of the Air & Waste Management Association, 57, 1014–1023,
777 <https://doi.org/10.3155/1047-3289.57.9.1014>, 2007.

778 Cuesta-Mosquera, A., Glojek, K., Močnik, G., Drinovec, L., Gregorič, A., Rigler, M.,
779 Ogrin, M., Romshoo, B., Weinhold, K., Merkel, M., Van Pinxteren, D., Herrmann,
780 H., Wiedensohler, A., Pöhlker, M., and Müller, T.: Optical properties and simple
781 forcing efficiency of the organic aerosols and black carbon emitted by residential
782 wood burning in rural central Europe, Atmos. Chem. Phys., 24, 2583–2605,
783 <https://doi.org/10.5194/acp-24-2583-2024>, 2024.

784 Dubovik, O., Holben, B., Eck, T. F., Smirnov, A., Kaufman, Y. J., King, M. D., Tanré,
785 D., and Slutsker, I.: Variability of Absorption and Optical Properties of Key
786 Aerosol Types Observed in Worldwide Locations, J. Atmos. Sci., 59, 590–608,
787 [https://doi.org/10.1175/1520-0469\(2002\)059<0590:VOAAOP>2.0.CO;2](https://doi.org/10.1175/1520-0469(2002)059<0590:VOAAOP>2.0.CO;2), 2002.

788 Dubovik, O. and King, M. D.: A flexible inversion algorithm for retrieval of aerosol
789 optical properties from Sun and sky radiance measurements, J. Geophys. Res., 105,
790 20673–20696, <https://doi.org/10.1029/2000JD900282>, 2000.

791 Dubovik, O., Sinyuk, A., Lapyonok, T., Holben, B. N., Mishchenko, M., Yang, P., Eck,
792 T. F., Volten, H., Muñoz, O., Veihelmann, B., Van Der Zande, W. J., Leon, J.,
793 Sorokin, M., and Slutsker, I.: Application of spheroid models to account for
794 aerosol particle nonsphericity in remote sensing of desert dust, J. Geophys. Res.,

795 111, 2005JD006619, <https://doi.org/10.1029/2005JD006619>, 2006.

796 García, O. E., Díaz, A. M., Expósito, F. J., Díaz, J. P., Dubovik, O., Dubuisson, P., Roger,
797 J. -C., Eck, T. F., Sinyuk, A., Derimian, Y., Dutton, E. G., Schafer, J. S., Holben,
798 B. N., and García, C. A.: Validation of AERONET estimates of atmospheric solar
799 fluxes and aerosol radiative forcing by ground-based broadband measurements, *J.*
800 *Geophys. Res.*, 113, 2008JD010211, <https://doi.org/10.1029/2008JD010211>, 2008.

801 Gliß, J., Mortier, A., Schulz, M., Andrews, E., Balkanski, Y., Bauer, S. E., Benedictow,
802 A. M. K., Bian, H., Checa-Garcia, R., Chin, M., Ginoux, P., Griesfeller, J. J.,
803 Heckel, A., Kipling, Z., Kirkevåg, A., Kokkola, H., Laj, P., Le Sager, P., Lund, M.
804 T., Lund Myhre, C., Matsui, H., Myhre, G., Neubauer, D., Van Noije, T., North, P.,
805 Olivié, D. J. L., Rémy, S., Sogacheva, L., Takemura, T., Tsigaridis, K., and Tsyro,
806 S. G.: AeroCom phase III multi-model evaluation of the aerosol life cycle and
807 optical properties using ground- and space-based remote sensing as well as surface
808 in situ observations, *Atmos. Chem. Phys.*, 21, 87–128,
809 <https://doi.org/10.5194/acp-21-87-2021>, 2021.

810 Guinot, B., Cachier, H., and Oikonomou, K.: Geochemical perspectives from a new
811 aerosol chemical mass closure, *Atmos. Chem. Phys.*, 7, 1657–1670,
812 <https://doi.org/10.5194/acp-7-1657-2007>, 2007.

813 Guo, J., Miao, Y., Zhang, Y., Liu, H., Li, Z., Zhang, W., He, J., Lou, M., Yan, Y., Bian,
814 L., and Zhai, P.: The climatology of planetary boundary layer height in China
815 derived from radiosonde and reanalysis data, *Atmos. Chem. Phys.*, 16, 13309–

816 13319, <https://doi.org/10.5194/acp-16-13309-2016>, 2016.

817 Gyawali, M., Arnott, W. P., Zaveri, R. A., Song, C., Moosmüller, H., Liu, L.,
818 Mishchenko, M. I., Chen, L.-W. A., Green, M. C., Watson, J. G., and Chow, J. C.:
819 Photoacoustic optical properties at UV, VIS, and near IR wavelengths for
820 laboratory generated and winter time ambient urban aerosols, *Atmos. Chem. Phys.*,
821 12, 2587–2601, <https://doi.org/10.5194/acp-12-2587-2012>, 2012.

822 Holben, B. N., Eck, T. F., Slutsker, I., Tanré, D., Buis, J. P., Setzer, A., Vermote, E.,
823 Reagan, J. A., Kaufman, Y. J., Nakajima, T., Lavenu, F., Jankowiak, I., and
824 Smirnov, A.: AERONET—A Federated Instrument Network and Data Archive for
825 Aerosol Characterization, *Remote Sensing of Environment*, 66, 1–16,
826 [https://doi.org/10.1016/S0034-4257\(98\)00031-5](https://doi.org/10.1016/S0034-4257(98)00031-5), 1998.

827 Intergovernmental Panel On Climate Change (Ipc): Climate Change 2021 – The
828 Physical Science Basis: Working Group I Contribution to the Sixth Assessment
829 Report of the Intergovernmental Panel on Climate Change, 1st ed., Cambridge
830 University Press, <https://doi.org/10.1017/9781009157896>, 2023.

831 Kirchstetter, T. W., Novakov, T., and Hobbs, P. V.: Evidence that the spectral
832 dependence of light absorption by aerosols is affected by organic carbon, *J.*
833 *Geophys. Res.*, 109, 2004JD004999, <https://doi.org/10.1029/2004JD004999>,
834 2004.

835 Kok, J. F., Ridley, D. A., Zhou, Q., Miller, R. L., Zhao, C., Heald, C. L., Ward, D. S.,
836 Albani, S., and Haustein, K.: Smaller desert dust cooling effect estimated from

837 analysis of dust size and abundance, *Nature Geosci*, 10, 274–278,
838 <https://doi.org/10.1038/ngeo2912>, 2017.

839 Lack, D. A. and Cappa, C. D.: Impact of brown and clear carbon on light absorption
840 enhancement, single scatter albedo and absorption wavelength dependence of
841 black carbon, *Atmos. Chem. Phys.*, 10, 4207–4220, [https://doi.org/10.5194/acp-](https://doi.org/10.5194/acp-10-4207-2010)
842 [10-4207-2010](https://doi.org/10.5194/acp-10-4207-2010), 2010.

843 Lack, D. A. and Langridge, J. M.: On the attribution of black and brown carbon light
844 absorption using the Ångström exponent, *Atmos. Chem. Phys.*, 13, 10535–10543,
845 <https://doi.org/10.5194/acp-13-10535-2013>, 2013.

846 Laskin, A., Laskin, J., and Nizkorodov, S. A.: Chemistry of Atmospheric Brown Carbon,
847 *Chem. Rev.*, 115, 4335–4382, <https://doi.org/10.1021/cr5006167>, 2015.

848 Lee, L. A., Reddington, C. L., and Carslaw, K. S.: On the relationship between aerosol
849 model uncertainty and radiative forcing uncertainty, *Proc. Natl. Acad. Sci. U.S.A.*,
850 113, 5820–5827, <https://doi.org/10.1073/pnas.1507050113>, 2016.

851 Lewis, K., Arnott, W. P., Moosmüller, H., and Wold, C. E.: Strong spectral variation of
852 biomass smoke light absorption and single scattering albedo observed with a novel
853 dual-wavelength photoacoustic instrument, *J. Geophys. Res.*, 113, 2007JD009699,
854 <https://doi.org/10.1029/2007JD009699>, 2008.

855 Li, J., Liu, C., Yin, Y., and Kumar, K. R.: Numerical investigation on the Ångström
856 exponent of black carbon aerosol, *J. Geophys. Res.*, 121, 3506–3518,
857 <https://doi.org/10.1002/2015JD024718>, 2016.

858 Li, J., Carlson, B. E., Yung, Y. L., Lv, D., Hansen, J., Penner, J. E., Liao, H.,
859 Ramaswamy, V., Kahn, R. A., Zhang, P., Dubovik, O., Ding, A., Lacis, A. A.,
860 Zhang, L., and Dong, Y.: Scattering and absorbing aerosols in the climate system,
861 *Nat Rev Earth Environ*, 3, 363–379, <https://doi.org/10.1038/s43017-022-00296-7>,
862 2022.

863 Li, L., Dubovik, O., Derimian, Y., Schuster, G. L., Lapyonok, T., Litvinov, P., Ducos,
864 F., Fuertes, D., Chen, C., Li, Z., Lopatin, A., Torres, B., and Che, H.: Retrieval of
865 aerosol components directly from satellite and ground-based measurements,
866 *Atmos. Chem. Phys.*, 19, 13409–13443, [https://doi.org/10.5194/acp-19-13409-](https://doi.org/10.5194/acp-19-13409-2019)
867 2019, 2019.

868 Li, W., Riemer, N., Xu, L., Wang, Y., Adachi, K., Shi, Z., Zhang, D., Zheng, Z., and
869 Laskin, A.: Microphysical properties of atmospheric soot and organic particles:
870 measurements, modeling, and impacts, *npj Clim Atmos Sci*, 7, 65,
871 <https://doi.org/10.1038/s41612-024-00610-8>, 2024.

872 Li, Y., Fu, T.-M., Yu, J. Z., Zhang, A., Yu, X., Ye, J., Zhu, L., Shen, H., Wang, C., Yang,
873 X., Tao, S., Chen, Q., Li, Y., Li, L., Che, H., and Heald, C. L.: Nitrogen dominates
874 global atmospheric organic aerosol absorption, *Science*, 387, 989–995,
875 <https://doi.org/10.1126/science.adr4473>, 2025.

876 Liu, C., Chung, C. E., Yin, Y., and Schnaiter, M.: The absorption Ångström exponent
877 of black carbon: from numerical aspects, *Atmos. Chem. Phys.*, 18, 6259–6273,
878 <https://doi.org/10.5194/acp-18-6259-2018>, 2018.

879 Luo, J., Li, Z., Qiu, J., Zhang, Y., Fan, C., Li, L., Wu, H., Zhou, P., Li, K., and Zhang,
880 Q.: The simulated source apportionment of light absorbing aerosols: Effects of
881 microphysical properties of partially-coated black carbon, *J. Geophys. Res.*, 128,
882 e2022JD037291, <https://doi.org/10.1029/2022JD037291>, 2023.

883 Luo, J., Li, D., Wang, Y., Sun, D., Hou, W., Ren, J., Wu, H., Zhou, P., and Qiu, J.:
884 Quantifying the effects of the microphysical properties of black carbon on the
885 determination of brown carbon using measurements at multiple wavelengths,
886 *Atmos. Chem. Phys.*, 24, 427–448, <https://doi.org/10.5194/acp-24-427-2024>,
887 2024.

888 Luo, J., Wang, W., Qiu, J., Zhang, Q., Li, C., Hou, W., Dong, X., and Hu, M.: Both non-
889 uniform mixing states and coating structures are important for absorption
890 enhancement and radiative effect of black carbon, *Opt. Express*, 33(10), 21719–
891 21735, <https://doi.org/10.1364/OE.552013>, 2025.

892 Malm, W. C., Sisler, J. F., Huffman, D., Eldred, R. A., and Cahill, T. A.: Spatial and
893 seasonal trends in particle concentration and optical extinction in the United States,
894 *J. Geophys. Res.*, 99, 1347–1370, <https://doi.org/10.1029/93JD02916>, 1994.

895 Moosmüller, H., Chakrabarty, R. K., Ehlers, K. M., and Arnott, W. P.: Absorption
896 Ångström coefficient, brown carbon, and aerosols: basic concepts, bulk matter,
897 and spherical particles, *Atmos. Chem. Phys.*, 11, 1217–1225,
898 <https://doi.org/10.5194/acp-11-1217-2011>, 2011.

899 Nishant, N., Sherwood, S. C., and Geoffroy, O.: Aerosol-induced modification of

900 organised convection and top-of-atmosphere radiation, *npj Clim Atmos Sci*, 2, 33,
901 <https://doi.org/10.1038/s41612-019-0089-1>, 2019.

902 Park, S., Son, S.-C., and Lee, S.: Characterization, sources, and light absorption of fine
903 organic aerosols during summer and winter at an urban site, *Atmospheric Research*,
904 213, 370–380, <https://doi.org/10.1016/j.atmosres.2018.06.017>, 2018.

905 Peng, K., Xin, J., Zhu, X., Wang, X., Cao, X., Ma, Y., Ren, X., Zhao, D., Cao, J., and
906 Wang, Z.: Machine learning model to accurately estimate the planetary boundary
907 layer height of Beijing urban area with ERA5 data, *Atmospheric Research*, 293,
908 106925, <https://doi.org/10.1016/j.atmosres.2023.106925>, 2023.

909 Petzold, A., Ogren, J. A., Fiebig, M., Laj, P., Li, S.-M., Baltensperger, U., Holzer-Popp,
910 T., Kinne, S., Pappalardo, G., Sugimoto, N., Wehrli, C., Wiedensohler, A., and
911 Zhang, X.-Y.: Recommendations for reporting “black carbon” measurements,
912 *Atmos. Chem. Phys.*, 13, 8365–8379, <https://doi.org/10.5194/acp-13-8365-2013>,
913 2013.

914 Ponczek, M., Franco, M. A., Carbone, S., Rizzo, L. V., Monteiro Dos Santos, D., Morais,
915 F. G., Duarte, A., Barbosa, H. M. J., and Artaxo, P.: Linking the chemical
916 composition and optical properties of biomass burning aerosols in Amazonia,
917 *Environ. Sci.: Atmos.*, 2, 252–269, <https://doi.org/10.1039/D1EA00055A>, 2022.

918 Russell, P. B., Bergstrom, R. W., Shinozuka, Y., Clarke, A. D., DeCarlo, P. F., Jimenez,
919 J. L., Livingston, J. M., Redemann, J., Dubovik, O., and Strawa, A.: Absorption
920 Angstrom Exponent in AERONET and related data as an indicator of aerosol

921 composition, *Atmos. Chem. Phys.*, 10, 1155–1169, <https://doi.org/10.5194/acp->
922 10-1155-2010, 2010.

923 Sand, M., Samset, B. H., Myhre, G., Gliß, J., Bauer, S. E., Bian, H., Chin, M., Checa-
924 Garcia, R., Ginoux, P., Kipling, Z., Kirkevåg, A., Kokkola, H., Le Sager, P., Lund,
925 M. T., Matsui, H., Van Noije, T., Olivié, D. J. L., Remy, S., Schulz, M., Stier, P.,
926 Stjern, C. W., Takemura, T., Tsigaridis, K., Tsyro, S. G., and Watson-Parris, D.:
927 Aerosol absorption in global models from AeroCom phase III, *Atmos. Chem.*
928 *Phys.*, 21, 15929–15947, <https://doi.org/10.5194/acp-21-15929-2021>, 2021.

929 Scarnato, B. V., Vahidinia, S., Richard, D. T., and Kirchstetter, T. W.: Effects of internal
930 mixing and aggregate morphology on optical properties of black carbon using a
931 discrete dipole approximation model, *Atmos. Chem. Phys.*, 13, 5089–5101,
932 <https://doi.org/10.5194/acp-13-5089-2013>, 2013.

933 Schuster, G. L., Dubovik, O., and Arola, A.: Remote sensing of soot carbon – Part 1:
934 Distinguishing different absorbing aerosol species, *Atmos. Chem. Phys.*, 16,
935 1565–1585, <https://doi.org/10.5194/acp-16-1565-2016>, 2016a.

936 Schuster, G. L., Dubovik, O., Arola, A., Eck, T. F., and Holben, B. N.: Remote sensing
937 of soot carbon – Part 2: Understanding the absorption Ångström exponent, *Atmos.*
938 *Chem. Phys.*, 16, 1587–1602, <https://doi.org/10.5194/acp-16-1587-2016>, 2016b.

939 Seinfeld, J. H., and Pandis, S. N.: *Atmospheric Chemistry and Physics: From Air*
940 *Pollution to Climate Change*, Wiley, 2016.

941 Shang, D., Hu, M., Zheng, J., Qin, Y., Du, Z., Li, M., Fang, J., Peng, J., Wu, Y., Lu, S.,

942 and Guo, S.: Particle number size distribution and new particle formation under
943 the influence of biomass burning at a high altitude background site at Mt. Yulong
944 (3410 m), China, *Atmos. Chem. Phys.*, 18, 15687–15703,
945 <https://doi.org/10.5194/acp-18-15687-2018>, 2018.

946 Sinyuk, A., Holben, B. N., Eck, T. F., Giles, D. M., Slutsker, I., Korokin, S., Schafer, J.
947 S., Smirnov, A., Sorokin, M., and Lyapustin, A.: The AERONET Version 3 aerosol
948 retrieval algorithm, associated uncertainties and comparisons to Version 2, *Atmos.*
949 *Meas. Tech.*, 13, 3375–3411, <https://doi.org/10.5194/amt-13-3375-2020>, 2020.

950 Sotiropoulou, R. E. P., Kaskaoutis, D. G., Kalkavouras, P., Grivas, G., Petrinoli, K.,
951 Garas, S. K., Liakakou, E., Tagaris, E., and Mihalopoulos, N.: Spatial variability
952 of carbonaceous aerosols and absorption characteristics between urban
953 background and residential sites during wintertime at a major Mediterranean city
954 (Athens; Greece), *Atmospheric Research*, 323, 108163,
955 <https://doi.org/10.1016/j.atmosres.2025.108163>, 2025.

956 Tao, C., Peng, Y., Zhang, Q., Zhang, Y., Gong, B., Wang, Q., and Wang, W.: Diagnosing
957 ozone–NO_x–VOC–aerosol sensitivity and uncovering causes of urban–nonurban
958 discrepancies in Shandong, China, using transformer-based estimations, *Atmos.*
959 *Chem. Phys.*, 24, 4177–4192, <https://doi.org/10.5194/acp-24-4177-2024>, 2024.

960 Tian, J., Wang, Q., Ni, H., Wang, M., Zhou, Y., Han, Y., Shen, Z., Pongpiachan, S.,
961 Zhang, N., Zhao, Z., Zhang, Q., Zhang, Y., Long, X., and Cao, J.: Emission
962 Characteristics of Primary Brown Carbon Absorption From Biomass and Coal

963 Burning: Development of an Optical Emission Inventory for China, *JGR*
964 *Atmospheres*, 124, 1879–1893, <https://doi.org/10.1029/2018JD029352>, 2019.

965 Tian, P., Zhang, L., Ma, J., Tang, K., Xu, L., Wang, Y., Cao, X., Liang, J., Ji, Y., Jiang,
966 J. H., Yung, Y. L., and Zhang, R.: Radiative absorption enhancement of dust mixed
967 with anthropogenic pollution over East Asia, *Atmos. Chem. Phys.*, 18, 7815–7825,
968 <https://doi.org/10.5194/acp-18-7815-2018>, 2018.

969 Tian, P., Zhang, N., Li, J., Fan, X., Guan, X., Lu, Y., Shi, J., Chang, Y., and Zhang, L.:
970 Potential influence of fine aerosol chemistry on the optical properties in a semi-
971 arid region, *Environmental Research*, 216, 114678,
972 <https://doi.org/10.1016/j.envres.2022.114678>, 2023.

973 Truex, T. J. and Anderson, J. E.: Mass monitoring of carbonaceous aerosols with a
974 spectrophone, *Atmospheric Environment* (1967), 13, 507–509,
975 [https://doi.org/10.1016/0004-6981\(79\)90143-4](https://doi.org/10.1016/0004-6981(79)90143-4), 1979.

976 Utry, N., Ajtai, T., Filep, Á., Pintér, M., Török, Zs., Bozóki, Z., and Szabó, G.:
977 Correlations between absorption Angström exponent (AAE) of wintertime
978 ambient urban aerosol and its physical and chemical properties, *Atmospheric*
979 *Environment*, 91, 52–59, <https://doi.org/10.1016/j.atmosenv.2014.03.047>, 2014.

980 Wang, L., Li, Z., Tian, Q., Ma, Y., Zhang, F., Zhang, Y., Li, D., Li, K., and Li, L.:
981 Estimate of aerosol absorbing components of black carbon, brown carbon, and
982 dust from ground-based remote sensing data of sun-sky radiometers, *JGR*
983 *Atmospheres*, 118, 6534–6543, <https://doi.org/10.1002/jgrd.50356>, 2013.

984 Wang, N., Wang, Y., Lu, C., Zhu, B., Yan, X., Sun, Y., Xu, J., Zhang, J., and Shen, Z.:
985 Interpretable ensemble learning unveils main aerosol optical properties in
986 predicting cloud condensation nuclei number concentration, *npj Clim Atmos Sci*,
987 8, 302, <https://doi.org/10.1038/s41612-025-01181-y>, 2025a.

988 Wang, Q., Ye, J., Wang, Y., Zhang, T., Ran, W., Wu, Y., Tian, J., Li, L., Zhou, Y., Hang
989 Ho, S. S., Dang, B., Zhang, Q., Zhang, R., Chen, Y., Zhu, C., and Cao, J.:
990 Wintertime Optical Properties of Primary and Secondary Brown Carbon at a
991 Regional Site in the North China Plain, *Environ. Sci. Technol.*, 53, 12389–12397,
992 <https://doi.org/10.1021/acs.est.9b03406>, 2019.

993 Wang, Q., Liu, H., Ye, J., Tian, J., Zhang, T., Zhang, Y., Liu, S., and Cao, J.: Estimating
994 Absorption Ångström Exponent of Black Carbon Aerosol by Coupling
995 Multiwavelength Absorption with Chemical Composition, *Environ. Sci. Technol.*
996 *Lett.*, 8, 121–127, <https://doi.org/10.1021/acs.estlett.0c00829>, 2021.

997 Wang, W., Tian, P., and Wu, Y.: Interpretable Machine Learning Quantifies
998 Composition and Size Controls on Aerosol Spectral Absorption,
999 <https://doi.org/10.5281/ZENODO.17852818>, 2025b.

1000 Wang, Y., Huang, R.-J., Zhong, H., Wang, T., Yang, L., Yuan, W., Xu, W., and An, Z.:
1001 Predictions of the Optical Properties of Brown Carbon Aerosol by Machine
1002 Learning with Typical Chromophores, *Environ. Sci. Technol.*, 58, 20588–20597,
1003 <https://doi.org/10.1021/acs.est.4c09031>, 2024.

1004 Wu, Y., Yan, P., Tian, P., Tao, J., Li, L., Chen, J., Zhang, Y., Cao, N., Chen, C., and

1005 Zhang, R.: Spectral Light Absorption of Ambient Aerosols in Urban Beijing during
1006 Summer: An Intercomparison of Measurements from a Range of Instruments,
1007 Aerosol Air Qual. Res., 15, 1178–1187, <https://doi.org/10.4209/aaqr.2014.09.0224>,
1008 2015.

1009 Yan, C., Zheng, M., Bosch, C., Andersson, A., Desyatnik, Y., Sullivan, A. P., Collett, J.
1010 L., Zhao, B., Wang, S., He, K., and Gustafsson, Ö.: Important fossil source
1011 contribution to brown carbon in Beijing during winter, Sci Rep, 7, 43182,
1012 <https://doi.org/10.1038/srep43182>, 2017.

1013 Yang, Z., Wang, Q., Wang, Q., Ma, N., Tian, J., Zhou, Y., Xu, G., Gao, M., Zhou, X.,
1014 Zhang, Y., Ran, W., Yang, N., Tao, J., Hong, J., Wu, Y., Cao, J., Su, H., and Cheng,
1015 Y.: Laboratory studies on the optical, physical, and chemical properties of fresh
1016 and aged biomass burning aerosols, <https://doi.org/10.5194/egusphere-2025-1020>,
1017 25 April 2025.

1018 Zhang, X., Li, L., Chen, C., Zheng, Y., Dubovik, O., Derimian, Y., Lopatin, A., Gui, K.,
1019 Wang, Y., Zhao, H., Liang, Y., Holben, B., Che, H., and Zhang, X.: Extensive
1020 characterization of aerosol optical properties and chemical component
1021 concentrations: Application of the GRASP/Component approach to long-term
1022 AERONET measurements, Science of The Total Environment, 812, 152553,
1023 <https://doi.org/10.1016/j.scitotenv.2021.152553>, 2022.

1024 Zhang, X., Mao, M., Yin, Y., and Tang, S.: The absorption Ångstrom exponent of black
1025 carbon with brown coatings: effects of aerosol microphysics and parameterization,

1026 Atmos. Chem. Phys., 20, 9701–9711, <https://doi.org/10.5194/acp-20-9701-2020>,
1027 2020.

1028 Zhang, X., Li, L., Che, H., Dubovik, O., Derimian, Y., Holben, B., Gupta, P., Eck, T. F.,
1029 Lind, E. S., Toledano, C., Xia, X., Zheng, Y., Gui, K., and Zhang, X.: Aerosol
1030 Components Derived from Global AERONET Measurements by GRASP: A New
1031 Value-Added Aerosol Component Global Dataset and Its Application, Bulletin of
1032 the American Meteorological Society, 105, E1822–E1848,
1033 <https://doi.org/10.1175/BAMS-D-23-0260.1>, 2024.

1034 Zhang, Z., Wang, Y., Chen, X., Xu, L., Zheng, Z., Ching, J., Zhu, S., Liu, D., and Li,
1035 W.: Absorption enhancement and shielding effect of brown organic coating on
1036 black carbon aerosols, npj Clim Atmos Sci, 8, 102,
1037 <https://doi.org/10.1038/s41612-025-00989-y>, 2025.

1038 Zhao, S., Hu, B., Du, C., Tang, L., Ma, Y., Liu, H., Zou, J., Liu, Z., Wei, J., and Wang,
1039 Y.: Aerosol optical characteristics and radiative forcing in urban Beijing,
1040 Atmospheric Environment, 212, 41–53,
1041 <https://doi.org/10.1016/j.atmosenv.2019.05.034>, 2019.